Aalto University
School of Science
Master's Programme in Engineering Physics

Antti Virtanen

ELMFIRE predictions of the bootstrap current profile in the JET pedestal region

Master's Thesis
Espoo, January 24, 2020

Supervisor: Professor Mathias Groth
Advisor: D.Sc. (Tech.) Timo Kiviniemi

Aalto University
School of Science
Master's Programme in Engineering Physics

ABSTRACT OF
MASTER'S THESIS

Author: Antti Virtanen

Title:
ELMFIRE predictions of the bootstrap current profile in the JET pedestal region

Date: January 24, 2020 **Pages:** v + 53

Major: Engineering Physics **Code:** SCI3056

Supervisor: Professor Mathias Groth

Advisor: D.Sc. (Tech.) Timo Kiviniemi

Magnetic confinement of a plasma in a tokamak fusion reactor requires sufficient plasma current drive to sustain the magnetic field configuration. In present devices, the necessary current is mainly driven by external means. Non-inductive, self-generated plasma current called bootstrap current is considered critical in any future tokamak-based designs. The bootstrap current develops in a plasma due to the presence of a radial plasma pressure gradient. Consequently, significant bootstrap current drive arises in particular in a steep pedestal that forms in high confinement mode plasma scenarios. The bootstrap current also plays an important role in pedestal stability.

In this thesis, the bootstrap current profile is studied in the pedestal region numerically with both neoclassical and turbulent simulations using plasma and magnetic parameters present in the JET tokamak. The simulations are performed with the gyrokinetic plasma simulation code ELMFIRE in the low-collisionality regime. The neoclassical simulation results are compared to two different analytical estimates. From the turbulence simulations, the effect of electrostatic instabilities on the bootstrap current profile is investigated by comparing the results to neoclassical predictions.

The neoclassical bootstrap current simulations are found to agree with the analytical estimates within a few percent. No large deviation between the two analytical models is observed for the low-collisionality regime, and both models match the simulation results within numerical accuracy, even when approaching the limit where the neoclassical approximations start to break down. However, discrepancies as large as 20% between the numerical simulation and the analytical estimates by the models are introduced when the collision grid used by ELMFIRE is made sparser, resulting in inaccuracy in the collision operator. The turbulence simulations show a strong effect of turbulent fluctuations on the plasma current which reduces the current density in comparison to the neoclassical predictions. Computational restrictions prevent further quantitative investigations and analyses.

Keywords: nuclear fusion, plasma, tokamak, bootstrap current

Language: English

Aalto-yliopisto
Perustieteiden korkeakoulu
Teknillisen fysiikan maisteriohjelma

DIPLOMITYÖN
TIIVISTELMÄ

Tekijä: Antti Virtanen

Työn nimi:
ELMFIRE:n ennustama bootstrap-virran profiili JET:n reuna-alueella

Päiväys:	24. tammikuuta 2020	**Sivumäärä:**	v + 53
Pääaine:	Teknillinen fysiikka	**Koodi:**	SCI3056
Valvoja:	Professori Mathias Groth		
Ohjaaja:	TkT Timo Kiviniemi		

Tokamak-fuusioreaktorin plasman magneettinen koossapito vaatii riittävän plasmavirran ylläpitämään reaktorin magneettikenttää. Nykyisissä laitteissa tarvittava virta luodaan pääasiassa ulkoisin keinoin. Tulevissa tokamakeissa induktioton ja itsestään plasmaan syntyvä bootstrap-virta on kuitenkin keskeinen tekijä. Bootstrap-virta syntyy plasmaan radiaalisen painegradientin vaikutuksesta. Varsinkin reuna-alueen plasmassa virta kehittyy merkittävän suuruiseksi, kun alueelle muodostuu jyrkän gradientin omaava kulkeutumiseste, joka johtaa korkeaan koossapitoon. Bootstrap-virralla on lisäksi tärkeä rooli reuna-alueen plasman vakaudessa.

Tässä työssä bootstrap-virran profiilia tutkitaan plasman reuna-alueella numeerisesti sekä neoklassisin että turbulentein simulaatioin käyttäen JET-tokamakin plasma- sekä magneettisia parametreja. Simulaatiot suoritetaan gyrokineettisellä ELMFIRE-plasmasimulaatiokoodilla matalan törmäyksellisyyden alueella. Neoklassisia tuloksia verrataan kahteen eri analyyttiseen malliin. Elektrostaattisten epävakaisuuksien vaikutusta bootstrap-virtaan tutkitaan vertaamalla turbulentin plasman simulaatiotuloksia neoklassisiin ennusteisiin.

Neoklassisten simulaatioiden havaitaan vastaavan analyyttisiä estimaatteja muutaman prosentin tarkkuudella. Matalan törmäyksellisyyden alueella analyyttisten mallien väliltä ei löydy suuria eroja. Molemmat mallit vastaavat simulaatioita numeerisen tarkkuuden rajoissa, jopa neoklassisen teorian rajoilla, jolloin mallien tekemät approksimaatiot eivät enää päde. Simuloidun bootstrap-virran ja analyyttisien mallien ennusteiden välille kuitenkin ilmaantuu jopa 20% eroavuuksia, kun ELMFIRE-koodin käyttämien törmäyshilakoppien määrää pienennetään, mikä aiheuttaa epätarkkuutta törmäysoperaattoriin. Turbulenteista simulaatioista havaitaan, että turbulenssi vaikuttaa voimakkaasti plasmavirtaan johtaen pienennettyyn virrantiheyteen neoklassisiin ennusteisiin verrattuna. Laskennalliset rajoitteet estävät kvantitatiivisempien tulosten keräämisen.

Asiasanat:	ydinfuusio, plasma, tokamak, bootstrap-virta
Kieli:	Englanti

Acknowledgements

I am thankful to my supervisor Mathias Groth for the opportunity to work in the Fusion group, and I would wish to thank Timo Kiviniemi for the instruction and guidance during the work, as well as the rest of the ELMFIRE group. Useful comments from Samuli Saarelma in EUROfusion Enabling Research meetings are also well appreciated.

The work has been supported by grant 316088 of the Academy of Finland. CSC – IT Center for Science, Finland, is gratefully acknowledged for computational resources.

Espoo, January 24, 2020

Antti Virtanen

Contents

Chapter 1

Introduction

Nuclear fusion is a potential candidate for a future energy source that could in principle replace fossil fuels and answer the rising global energy demand. Fusion reactions that convert hydrogen into helium are the source of power of stars, such as the Sun, and they release substantial amounts of energy. On Earth, the fuel resources for fusion power production are also plentiful and can be found essentially everywhere. Fusion is sustainable regarding natural resources and environment as well because nuclear fusion reactions produce no greenhouse gases. Achieving controlled nuclear fusion for practical power generation is, however, not without challenges. The necessary conditions are demanding. First, the temperature of the fuel has to be extremely high, in excess of 100 million °C, which turns the fuel into a plasma. Additionally, high particle density and sufficiently long energy confinement time are needed to enable fusion reactions to take place.

In laboratory conditions, the hot plasma can be contained in a thermonuclear fusion reactor, such as a tokamak [1], with magnetic confinement. Unfortunately, the plasma confinement time is restricted by flow of particles and heat radially out of the main tokamak plasma, which is governed by complex turbulent transport driven by plasma instabilities. However, a transition to high confinement mode (H-mode) regime was observed in fusion experiments [2]. During this transition, a steep pressure gradient forms in the plasma near the plasma edge where the temperature and particle density decrease radially outwards sharply over a narrow region. This characteristic in the plasma profile is called an edge pedestal. In the improved confinement state, plasmas exhibit a reduced number of instabilities and diminished energy losses. Instabilities reduce reactor performance, and therefore, finding a stable plasma configuration is essential.

In a tokamak, a toroidal plasma current generates a poloidal magnetic field inside the device which provides confinement. A significant part of this plasma

current is generated with a transformer. However, a self-generated current called the bootstrap current is also produced intrinsically due to the plasma itself. The bootstrap current is driven by the radial plasma pressure gradient, and large currents therefore form especially at the steep edge pedestal. The bootstrap current plays an important role in any future tokamak design that strives to be economical. If the current required for confinement is mostly provided by the bootstrap current, then minimal external current drive sources are needed. Particularly, the transformer action is a weakness in the present pulsed tokamak designs as it prevents steady state operation. Although a large bootstrap current is vital in future tokamaks, it has been discovered also to have a complex effect on plasma stability [3]. In the pedestal region, high current improves the stability by altering the magnetic shear, but as a downside, it can also drive other plasma instabilities.

Studying complicated physical phenomena requires high-performance computing and massively parallel computers. In fusion research, computational work is especially important because performing experiments is expensive. Computer simulations can reveal new information about the physics involved, for example, regarding plasma dynamics and transport. Code predictions also facilitate development of more accurate analytical formulas and allow optimizing experiments. Regarding the bootstrap current at the steep edge pedestal, predictive simulations and accurate modeling are important in understanding the plasma behavior. As the current gets large, then even slight changes in its magnitude can significantly affect the pedestal region.

1.1 Problem statement

The aim of this thesis is to study the bootstrap current profile in the presence of a steep edge pedestal in a tokamak plasma with the gyrokinetic code ELMFIRE. The simulation parameters used correspond to pedestal conditions in the Joint European Torus (JET). The performed simulations include both neoclassical and turbulent runs. The predictions from the neoclassical studies are compared to estimates by well-established analytical models. Also, the effect of non-locality in the neoclassical limit and the numerical accuracy of the simulations is tested. By allowing instabilities to form in the plasma, the effect of turbulence on the predicted bootstrap current is considered as well as the level of turbulent diffusion relative to neoclassical. All the simulations described are performed in the low-collisionality banana regime which is typical for JET pedestal region.

1.2 Structure of the thesis

The thesis is organized as follows. The basics of thermonuclear fusion and plasma transport are discussed in chapter 2. The transport mechanisms discussed include neoclassical and turbulence driven transport. Formation of the bootstrap current in a tokamak device and the analytical formulas used in this thesis to predict it are introduced in chapter 3. The fundamentals of the ELMFIRE simulation code are described in chapter 4. Chapter 5 discusses the simulation results, and finally, the conclusions are presented in chapter 6. In appendix A, the guiding center equations of motion for the simulated particle orbits are derived.

Chapter 2

Plasma physics

2.1 Nuclear fusion and plasmas

In nuclear fusion, light atomic nuclei bind together to form a single heavier nucleus and consequently release energy. The released energy represents the difference in mass between the fused nucleus and its individual constituents. For a single reaction, the energy density is high even compared to nuclear fission which makes fusion an ample energy source. The most prominent nuclear fusion reaction candidate for future fusion energy production is between the two hydrogen isotopes deuterium (D) and tritium (T)

$$ {}^{2}_{1}\mathrm{D} + {}^{3}_{1}\mathrm{T} \rightarrow {}^{4}_{2}\mathrm{He} + {}^{1}_{0}\mathrm{n} + 17.6 \text{ MeV}, $$

in which the two nuclei fuse into a helium nucleus (He) [4]. In this process, a neutron (n) is emitted and 17.6 MeV energy is released as kinetic energy of the reaction products. Most of the released energy (14.1 MeV) is carried by the neutron.

In thermonuclear fusion, the binding of nuclei is achieved by colliding the particles together at such a high temperature that their kinetic energy overcomes the Coulomb barrier which keeps the positive charges apart. Thermonuclear fusion requires extremely high temperatures that cause the fusing particle species to exist as a plasma. Plasma is a state of matter that forms from a gas when atoms are stripped of their electrons. Thus, plasma consists of unbound positively charged ions and negatively charged electrons. On small scale, plasma particles interact with each other through small-angle binary Coulomb collisions. At larger scale, the charged particles interact collectively via Coulomb interactions that have virtually infinite range. Due to the long-range interactions, any charge separation occurring in the plasma will tend to cancel by a strong restoring force resulting in the plasma to remain quasineutral.

2.2 The tokamak concept

One way to achieve controlled nuclear fusion and harness the fusion energy in a laboratory environment is magnetic plasma confinement. Magnetic confinement has become the main concept in fusion research, and the most successful device designed for this approach is the tokamak. A tokamak is a thermonuclear fusion reactor shaped as a torus. The reactor chamber of a tokamak is a vacuum vessel in which the motion of the hot plasma is constrained with strong magnetic fields to protect the material walls from contact with the plasma. Avoiding plasma-wall interactions also prevents unwanted impurities from polluting the plasma which would lead to fuel dilution, plasma performance reduction, and quenching of the fusion reactions. The magnetic field is shaped with the purpose to provide control over the plasma and consequently to achieve plasma equilibrium and stability.

The tokamak has a helical magnetic field configuration inside the vessel consisting of a toroidal (B_t) and a poloidal (B_p) field component (Fig. 2.1). In the presence of the magnetic field, the charged plasma particles are confined to the helical field lines, travelling along them in a gyrating motion. The spiraling

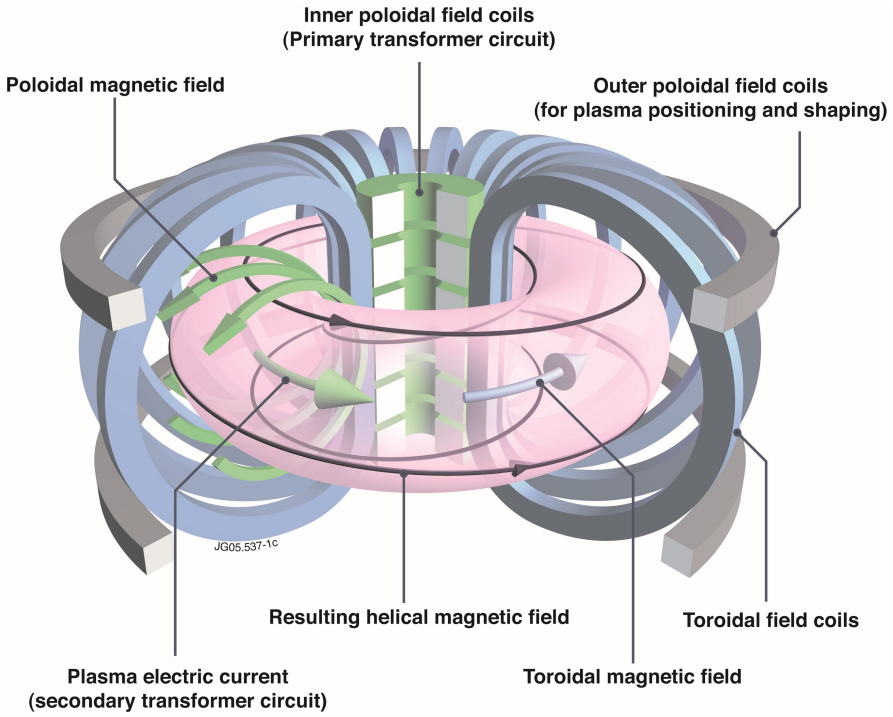

Figure 2.1: Schematic picture of a tokamak illustrating the magnetic field structure. Figure courtesy to EUROfusion: https://www.euro-fusion.org.

field lines do not cross each other and together they form nested magnetic flux surfaces with a magnetic axis in the center. The field is produced with a set of coils. The toroidal field in the direction toroidally along the torus is generated with coils wrapped around the tokamak uniformly spaced. These coils are more closely packed at the center of the torus compared to the edge which makes the magnetic field stronger near the center. The poloidal field circulating the torus the short way around is generated with a toroidal electric current driven by induction in the highly conductive plasma itself. This is accomplished with a central solenoid in the middle of the torus. The solenoid acts as the primary transformer circuit of an ohmic transformer while the plasma acts as the secondary circuit. The induced toroidal electric field driving the plasma current is proportional to the time rate of change of the current being gradually increased in the primary circuit. However, the current cannot be increased indefinitely making the tokamak inherently a pulsed device. Additionally, a set of poloidal field coils further position and shape the plasma.

2.3 Core plasma transport

Understanding the mechanisms of particle, momentum, and energy transport in the main plasma enables one to explain plasma physics phenomena encountered in present tokamaks and predict the plasma behavior in different plasma scenarios and in future reactors. In a magnetic field, plasma particles will tend to move freely along the magnetic field lines they are constrained to. However, this parallel movement gets interrupted due to collisions between the particles that result in perpendicular transport across field lines.

Classical plasma transport theory is based on Coulomb collisions between the charged plasma particles in a straight magnetic field [5]. In this case, particle diffusion through collisions can be modeled as a random walk process which is sufficient to describe particle and heat fluxes in the system. The Coulomb collisions are small-angle collisions with the collisional steps being small deflections. Thus, it is appropriate to describe the collisions in a plasma with the time it takes for a particle to accumulate a total of 90-degree scattering which can be considered significant. For collisions between particle species α and β this collision time is $\tau_{\alpha\beta}$ and the related collision frequency is

$$\nu_{\alpha\beta} = \frac{1}{\tau_{\alpha\beta}} = \frac{Z_\alpha^2 Z_\beta^2 e^4 n_\beta \ln\Lambda}{3\pi^{3/2}\epsilon_0^2 m_\alpha^2 v_{\mathrm{th}}^3} \tag{2.1}$$

where Z is the charge number, e is the elementary charge, n is the particle density, $\ln\Lambda$ is the Coulomb logarithm, ϵ_0 is the vacuum permittivity, m

is the mass, and $v_{\text{th}} = \sqrt{2T/m}$ is the thermal speed with T being the temperature. The Coulomb logarithm is defined in the Naval Research Laboratory (NRL) plasma formulary [6] for collisions between different particle species. Classically, perpendicular diffusion resulting from collisions has a step size of the order of the particle gyroradius, which is also called the Larmor radius. The Larmor radius is defined as $\rho = v_{\text{th}}/\Omega$ where $\Omega = qB/m$ is the gyrofrequency of the particle with $q = Ze$ being its charge and B is the magnetic field strength.

2.3.1 Neoclassical transport

In tokamaks, the collisional plasma transport is enhanced due to toroidal effects. This is described by neoclassical transport theory [5]. The curved magnetic field geometry and its gradients modify the particle orbits by creating drifts that shift them from the magnetic flux surfaces resulting in increased diffusion step size.

In addition to particles that follow the magnetic field lines around the torus of a tokamak, called passing particles, there are magnetically trapped particles. Trapped orbits are created due to the conservation of energy and magnetic moment of the charged plasma particles. First, the conservation of kinetic energy $E = mv^2/2$ implies that the total speed of the particle $v^2 = v_\parallel^2 + v_\perp^2$ is conserved throughout the particle orbit. The velocity components are oriented parallel ($v_\parallel$) and perpendicular ($v_\perp$) to the magnetic field direction. Second, the conservation of magnetic moment $\mu = mv_\perp^2/(2B)$, which is an adiabatic invariant, shows that as the magnetic field strength increases toward the inboard side of the torus during a particle orbit, the perpendicular velocity of the particle must increase accordingly. This in turn results in decreasing the parallel velocity of the particle in order to preserve its total speed. If a particle has sufficiently small parallel velocity with respect to the magnetic field lines, the particle gets magnetically mirrored at the boundary between the stronger and weaker magnetic fields. This process results in the particle oscillating on the outboard side of the torus between two bouncing points. The trapped orbit with the bounces and vertical guiding center drifts resembles the shape of a banana in the poloidal cross section. The width of the trapped orbit is called the banana width and the time to complete an oscillation is called the banana time or the bounce time. The trapped particles diffuse with step size comparable to the banana width rather than the smaller Larmor radius which enhances their diffusivity compared to classical transport.

The neoclassical transport depends on the ion collisionality which describes how many collisions a trapped particle experiences during the time it takes to bounce between the turning points of its banana orbit. The collisionality

is defined as

$$\nu_{i*} = \frac{\nu_{i,\text{eff}}}{\omega_b} = \frac{\nu_{ii} R_0 q_s}{v_{i,\text{th}} \epsilon^{3/2}} \tag{2.2}$$

where $\nu_{i,\text{eff}} = \nu_{ii}/\epsilon$ is the effective collision frequency of ions and $\omega_b = v_{i,\text{th}}\sqrt{\epsilon}/(R_0 q_s)$ is the bounce frequency with $\epsilon = r/R_0$ being the local inverse aspect ratio of the tokamak, r being the local minor radius, a radial coordinate from the magnetic axis to the plasma edge, R_0 being the major radius of the tokamak at the magnetic axis, and $q_s = \epsilon B_t/B_p$ is the safety factor.

Based on the magnitude of the collisionality, neoclassical transport theory can be divided into three different transport regimes. These regimes are the banana regime $\nu_{i*} < 1$, the plateau regime $1 \leq \nu_{i*} \leq \epsilon^{-3/2}$, and the Pfirsch-Schlüter regime $\nu_{i*} > \epsilon^{-3/2}$ [7]. In the banana regime, the collisionality is small enough for both the passing and trapped particles to complete their orbits before being scattered in a collision. The fact that trapped orbits exist at this low collisionality gives the banana regime its name. In the plateau regime, the effective collision frequency is greater than the bounce frequency, and therefore, trapped particles get scattered into passing particles before completing an orbit. The fast circulating passing particles, however, are still able to complete their orbits before they scatter. In contrast, in the Pfirsch-Schlüter regime, passing and trapped particles no longer complete full orbits because of the high collisionality preventing it. The neoclassical particle diffusivity is proportional to the collisionality in the banana and Pfirsch-Schlüter regimes where the diffusivity grows together with increasing collisionality. In the plateau regime, however, diffusivity has no collisionality dependence and it is assumed to remain at a constant level, hence the name plateau.

Neoclassical transport theory assumes locality. Locality is defined by the ratio of the ion banana orbit width and the plasma background scale lengths, which are assumed smaller than unity, $\rho_p/L_{n,T} \ll 1$ [7]. The ion banana orbit width is approximated by ion poloidal Larmor radius defined as $\rho_p = v_{i,\text{th}}/\Omega_p$ where $\Omega_p = q_i B_p/m_i$ is the ion poloidal gyrofrequency. The plasma background is characterized by radial gradient scale lengths which are defined as $L_n = |n/\nabla n|$ and $L_T = |T/\nabla T|$ for density and temperature profiles, respectively. The ions have larger orbits than the electrons because of their larger mass, and hence, it is sufficient to test this neoclassical limit for the ion orbit width. In the local regime, the plasma particles will not experience large changes in the background while orbiting.

2.3.2 Turbulent transport

Not all of the energy and particle transport observed in tokamaks can be explained with the collisional transport theory. In experiments, particle and heat losses resulting from radial transport across magnetic flux surfaces and out of the main plasma have been measured to be orders of magnitude larger than predicted by neoclassical theory. These anomalous losses are turbulent by nature. However, even though turbulence dominates the transport, the neoclassical effects and phenomena can be important in operating tokamaks and the transport predicted by neoclassical theory is thus not completely irrelevant. Furthermore, neoclassical theory has been observed to adequately explain plasma behavior of some quantities in enhanced-confinement H-mode plasmas in which turbulent fluctuations are significantly reduced, e.g. of ion heat diffusivity [8].

Turbulence-induced transport results from micro-instabilities, also called modes. These modes are driven unstable by steep gradients encountered especially in the plasma edge when a pedestal is formed. The gradients act as a source of free energy which drive these instabilities. The unstable modes strengthen perturbations in the plasma and consequently drive outflow of particles and energy once initialized. Two electrostatic micro-instabilities that are considered as potential candidates for enhanced turbulent transport in the tokamak main plasma are ion temperature gradient (ITG) mode and trapped electron mode (TEM) [9]. Both micro-instabilities have scale lengths comparable to the ion Larmor radius.

Turbulence is extremely disadvantageous in magnetized tokamak plasmas because it reduces energy confinement. Additionally, high radial transport due to turbulent fluctuations can extend to the tokamak walls and cause significant plasma-wall interactions. Therefore, understanding plasma turbulence and controlling this highly non-linear transport is essential for improving confinement and achieving controlled thermonuclear fusion.

In addition to radial transport, turbulence also affects the particle flow parallel to the magnetic field. Three different mechanisms for turbulent parallel flow are addressed when focusing only on electrostatic perturbations contributing to the turbulence [10]. The first one being the electron residual Reynolds stress which contributes to the parallel electron momentum flux and drives parallel electron flow. The residual stress experiences rapid spatial variation and creates large local electromotive force in the plasma, which drives fine scale corrugations in the plasma current profile. Although this results in large localized deviations, a non-vanishing net deviation in the current profile is expected on average. Another mechanism is the acceleration of electron parallel flow through momentum exchange between ions and electrons

mediated by turbulence. The average effect of this anomalous momentum exchange can be comparable to the averaged electron residual stress, and it also drives a net deviation in current. The third mechanism arises from the toroidal geometry of a tokamak, and it is the turbulent equivalent to the bootstrap current mechanism described more closely in the next chapter.

Chapter 3

Bootstrap current

The bootstrap current is a self-generated current parallel to the magnetic field in toroidal geometries which is predicted by neoclassical transport theory. This current plays an important role considering plasma confinement. As a parallel current, the bootstrap current contributes to the total toroidal plasma current that sustains the magnetic equilibrium of a tokamak. Unlike the ohmic current generated in the plasma with a transformer, the bootstrap current is non-inductive and develops naturally in the presence of a radial pressure gradient. It has been experimentally confirmed in several devices [11, 12]. The significance of the bootstrap current for tokamak operation comes from the fact that it has the potential to provide the majority of the plasma current required to generate the poloidal magnetic field component. Thus, the bootstrap current possibly gives rise to a more economical steady state tokamak in the future with no inductive current drive and only minimal external drive by other means [13].

The bootstrap current originates from the trapped particles with finite banana orbit widths, and it is driven by the plasma pressure gradient that depends on radial density and temperature gradients [14]. Guiding center drifts shift particle orbits from the magnetic flux surfaces according to neoclassical physics, and therefore, the trapped particles deviate from a flux surface by a banana width while orbiting. Considering two trapped ions that start their orbits from the same magnetic flux surface but move in the opposite directions, their banana orbits reside on different sides of the flux surface due to the drifts they experience (Fig. 3.1). The particles are more densely packed in the center of the plasma, and the temperature in the core is greater than at the edge, which results in density and temperature gradients. Due to these gradients, there are more particles occupying the banana orbit on the inside of the flux surface rather than on the outside. Furthermore, the plasma particles on the inner orbit have higher velocity. The particles on

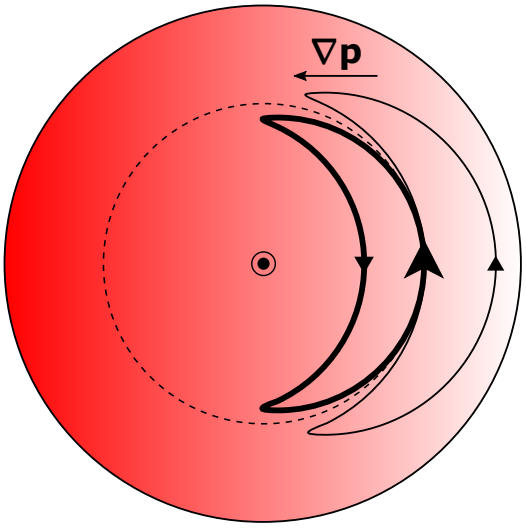

Figure 3.1: Origin of the bootstrap current from trapped particle motion. The guiding center orbits of trapped particles are projected on the poloidal plane. The particle density as well as the temperature are larger on the inner orbit near the magnetic axis shown in the middle, and the pressure gradient is in the same direction. The bootstrap current is in the direction shown in between the two orbits. The dashed line represents a magnetic flux surface.

the outer branch of their banana orbits carry current in the plasma current direction. Hence, the particles orbiting on the inside of the considered flux surface are all moving in the co-current direction on that flux surface while the particles orbiting on the outside move in the counter-current direction. This asymmetry in the co- and counter-moving particle distributions causes a net current on the magnetic flux surface in the plasma current direction, which is called the banana current. In addition, while ions and electrons have opposite charge, they also drift in opposite directions, and therefore, their contributions to the current add together.

The banana current is only a small fraction of the actual bootstrap current but it is critical for generating the main part. The trapped and passing plasma particles are collisionally coupled and they establish a collisional equilibrium. In the collisions, momentum is passed from the trapped particles to the passing ones. The trapped particles accelerate the passing particles on a given flux surface in their own direction, and because there are more trapped particles flowing in the direction of the plasma current, the passing particles moving in the co-current direction also dominate. The bootstrap current is mostly carried by the more freely moving passing particles [7]. It can be deduced that the bootstrap current arises in a sufficiently collisionless plasma

where there are trapped particles present. However, the collisionality cannot be exactly zero in order to enable frictional momentum exchange between the particles. Typically, the electrons contribute more to the bootstrap current than the ions.

Understanding the bootstrap current is crucial considering plasma stability, especially in the pedestal region. Radial profile gradients can become large when a steep pedestal forms in the plasma during transition to H-mode, and these sharp gradients are capable of driving strong bootstrap current. Recognising the effects that the bootstrap current has on the edge equilibrium and stability require careful study of its behavior through accurate modeling and simulation.

3.1 Sauter model

A formula developed by Sauter et al. [15, 16] has been widely used in the study of bootstrap current density in tokamaks. The motivation for the formulation was to describe the bootstrap current under realistic conditions. Hence, the Sauter formula is compatible with a variety of different flux surface geometries describing the magnetic field equilibrium, and it makes no assumptions regarding the plasma collisionality. The model is a good approximation for conventional tokamak operating conditions in the local regime.

An expression for the bootstrap current can be derived starting from the parallel momentum and heat flux balance equations [17, 18]. This system of equations is solved to obtain an expression for parallel fluid flow which is further used for formulating the parallel bootstrap current density. The transfer of momentum between particles and the effects of collisionality are incorporated via friction and viscosity coefficients. This procedure described above is a general approach for solving the bootstrap current density and it serves as the basis for the Sauter formula as well. However, in the Sauter model, the collisional effects were incorporated into the formalism by numerical consideration utilizing a full linearized collision operator. The flux surface averaged and magnetic field weighted bootstrap current density, j_{bs}, according to the Sauter model is given by

$$\langle j_{\mathrm{bs}} B \rangle = -I(\psi) p_e \left[L_{31} \frac{p}{p_e} \frac{\partial \ln p}{\partial \psi} + L_{32} \frac{\partial \ln T_e}{\partial \psi} + L_{34} \alpha \frac{T_i}{Z_{\mathrm{eff}} T_e} \frac{\partial \ln T_i}{\partial \psi} \right] \tag{3.1}$$

where $\langle \cdot \rangle$ denotes the flux surface average, $I(\psi) = R_0 B_{\mathrm{t}}$ is a constant flux function, ψ is the poloidal magnetic flux, $p = p_e + p_i$ is the total plasma pressure with $p_s = n_s T_s$ being the plasma pressure of species s, and $Z_{\mathrm{eff}} = \sum_k n_k Z_k^2 / n_e$

is the effective ion charge with k being the ion species index. The gradients in terms of the poloidal flux are related to radial gradients by $\partial X/\partial\psi = (R_0 B_p)^{-1}\partial X/\partial r$ in a circular tokamak approximation with a large aspect ratio. In front of the gradients in the current density definition are fitted coefficients, which were determined from numerical simulation results. The transport coefficients L_{3j} are functions of effective charge Z_{eff}, trapped particle fraction f_t and electron collisionality ν_{e*}, and the ion flow coefficient α is a function of trapped particle fraction f_t and ion collisionality ν_{i*}. Analytical expressions for these coefficients are presented in Refs. [15, 16]. The bootstrap current density alone is obtained from the given expression as $j_{\text{bs}} = \langle j_{\text{bs}} B\rangle / B_0$ where B_0 is the magnetic field strength on the magnetic axis.

The assumed locality causes the Sauter formula to be accurate solely within the neoclassical limit. The neoclassical assumptions start to break down near the plasma edge, where typically steep gradients are encountered. Inaccuracies of the model have been reported regarding bootstrap current predictions in the steep pedestal region [19–21].

3.2 Hager model

A more recent formula introduced by Hager et al. [21] for modeling the bootstrap current density profile was developed particularly for studying the edge pedestal. The model aimed to establish understanding of the pedestal bootstrap current while the previous works were based on limiting approximations that are not valid in the pedestal region. The Hager model is based on the Sauter formula in equation (3.1) which is modified with several corrections that allow this improved model to be used in the non-local regime as well where particles experience finite orbit width effects. The Sauter model is likely to overestimate j_{bs} compared to predictions that take into account the regions where the width of trapped ion banana orbits are of the order of the gradient scale lengths. Additionally, the collisionality in the pedestal region is high compared to the plasma center and can become significant for the bootstrap current density. The Hager formula more accurately takes into account collisional effects.

The analytical formula introduced in the study by Hager et al. [21] was constructed based on global numerical simulation results obtained from modeling the behavior of the entire tokamak plasma in the torus geometry. The Hager model utilizes a fully non-linear collision operator in formulating the bootstrap current coefficients. The bootstrap current density according

to the Hager model is given by

$$\begin{aligned}\langle j_{\mathrm{bs}}B\rangle = &-(\beta_{\mathrm{col}}+\beta_{\nabla T_i})I(\psi)p_e\Bigg[\gamma_{31}L_{31}\frac{p}{p_e}\frac{\partial \ln p}{\partial \psi}\\ &+\gamma_{32}L_{32}\frac{\partial \ln T_e}{\partial \psi}+(\gamma_{34}L_{34})(\gamma_\alpha\alpha)\frac{T_i}{Z_{\mathrm{eff}}T_e}\\ &\times\left(1-2\Delta_\psi\left(-\frac{3}{2}L_{T_i}^{-1}+L_n^{-1}+L_q^{-1}\right)\right)\frac{\partial \ln T_i}{\partial \psi}\Bigg]\end{aligned} \tag{3.2}$$

where β_{col}, $\beta_{\nabla T_i}$, γ_{3j}, and γ_α are correction terms presented in Ref. [21] together with the modification to L_{34} in the last term shown inside the parentheses. In addition, $\Delta_\psi = Iv_\parallel/\Omega$ is the ion orbit width in units of poloidal flux and $L_X^{-1} = X^{-1}\partial X/\partial\psi$ represents a gradient scale length that is required for the ion temperature, plasma density, and safety factor.

The term β_{col} is a collisional damping factor that corrects the Sauter formula by taking into account the increased collisionality encountered at the edge pedestal. β_{col} depends on electron collisionality ν_{e*} and the inverse aspect ratio ϵ, and in large-aspect-ratio tokamaks its value gets close to one. These dependencies are defined using several optimized fitting parameters in the damping factor which are listed in Ref. [21], and the same parameter values were used in this work.

The coefficients γ_{3j} and γ_α correct the asymptotic behavior of the bootstrap current at the collisional regime. The transport coefficients L_{3j} depend on the trapped particle fractions f_{t} and on the electron collisionality ν_{e*}. In the Sauter equation, L_{3j} depend on collisionality through ν_{e*}^{-1} [15], but according to neoclassical theory, L_{3j} should instead decay with order ν_{e*}^{-2} when $\nu_{e*} \gg 1$ [7]. This inaccuracy in the collisional limit was corrected in the Hager equation by combining the Sauter formula with another bootstrap current equation by Helander et al. [5], which includes the correct asymptotic behavior. The interpolation coefficients γ_{3j} control at which collisionality the transport coefficients by Sauter will switch on the appropriate asymptotic behavior and transition to the coefficients by Helander. Similar transition to Helander's coefficient is performed for the ion flow coefficient α with the interpolation coefficient γ_α.

One of the introduced corrections modifies L_{34}. It takes into account the changes in the safety factor and collision frequency of ions during the ion orbits, and thus, it signifies correction to the bootstrap current due to finite ion orbit width. Within a steep pedestal, ions can experience different plasma conditions at different parts of their orbits. Another correction term for the finite ion orbit width is $\beta_{\nabla T_i}$ which damps the bootstrap current similar to β_{col}. The term $\beta_{\nabla T_i}$ depends on the ion collisionality ν_{i*}, the inverse aspect ratio ϵ,

the ion orbit width Δ_ψ, and the ion temperature gradient scale length $L_{T_i}^{-1}$. In addition, the term incorporates the Shafranov shift $\Delta_R = \partial R_c/\partial r$, where R_c is the geometrical center of a magnetic flux surface, into the bootstrap current equation. In a toroidal geometry, the plasma pressure expands the plasma outwards and thus pushes the magnetic flux surfaces closer together at the outboard side of the torus. The Shafranov shift describes a resulting deviation of the magnetic axis radially outwards from the geometrical center of the plasma. Also, $\beta_{\nabla T_i}$ includes several fitted parameters as did β_{col}. The same parameter values as reported in Ref. [21] are used here.

The study of the bootstrap current behavior in the edge pedestal has revealed significant differences compared to the core plasma. Typically, the majority of the bootstrap current is carried by untrapped passing particles. However, the relative contribution from trapped electrons was observed to increase while the passing electron contribution was suppressed at the plasma edge within the pedestal [21]. The passing particle population at the edge is small compared to the core plasma, and the large amount of collisions experienced at the edge pedestal further reduce the relative contribution of passing electrons compared to the trapped electrons. This is because of the friction of passing electron current with ions at the collisional regime which reduces the passing electron current relative to the trapped electron current.

3.3 Turbulent analogue of bootstrap current

Turbulence is capable of altering the plasma current. The turbulent fluctuations modify plasma density and temperature profiles, and thus, affect the plasma current drive; they also affect electron current directly. A turbulent electron current drive mechanism in which particles are scattered by wave-particle interactions instead of collisions has an analogous principle to the bootstrap current drive associated with neoclassical transport.

The neoclassical bootstrap current is for the most part driven by passing electrons when a collisional equilibrium has been established between trapped and passing particles. A similar but collisionless equilibrium forms in the plasma via electron detrapping by turbulence. The turbulence-induced detrapping results from pitch angle scattering caused by wave-particle resonances, along with a contribution from radial transport introduced by the plasma instabilities [22]. The pitch angle describes the ratio between the parallel and perpendicular particle velocity components, and when this angle is modified, the particle scatters.

The turbulent current drive mechanisms cause deviations from the neoclassical predictions. The relative strength of the contributing collisional transport

and micro-instability driven turbulent transport can be approximated by a simplified formula given in [22]

$$\frac{D^{QL}}{D^{\text{neo}}} \sim \sqrt{\frac{m_e}{m_i}}\left(\frac{q_s}{\epsilon^{5/2}}\right)\left(\frac{L_n}{R_0}\right)\left(\frac{v_e}{v_{\text{e,th}}}\right)^3 \frac{1}{\nu_{e*}}\left|\frac{e\delta\Phi}{T_e}\right|^2 \tag{3.3}$$

where D^{QL} is a quasilinear diffusion coefficient corresponding to the turbulent transport by pitch angle scattering, D^{neo} is a neoclassical diffusion coefficient corresponding to the collisional transport, and $|e\delta\Phi/T_e|$ is the amplitude of the turbulent fluctuations with $\delta\Phi$ denoting the fluctuation of the electrostatic potential.

Chapter 4

ELMFIRE

ELMFIRE is a full-f gyrokinetic numerical simulation code capable of simulating both neoclassical and turbulent particle transport in the tokamak geometry. The code simulates a tokamak plasma by self-consistently solving the time evolution of the full particle distribution function (full-f) with a particle-in-cell (PIC) method. Some features of the code are covered below but a more extensive and detailed description is presented in Ref. [23] and the latest upgrades in Ref. [24].

The geometry of the simulation configuration in ELMFIRE is that of an axisymmetric circular tokamak. The circular magnetic flux surfaces on a poloidal cross section are concentric. The magnetic field equilibrium geometry is given by

$$\boldsymbol{B} = (B_t \hat{\boldsymbol{e}}_t + B_p(r)\hat{\boldsymbol{e}}_p)\frac{R_0}{R} \tag{4.1}$$

in which the toroidal magnetic field component is determined to be a constant B_t on the magnetic axis, and the poloidal component is a function of the radial coordinate and defined as $B_p(r) = \sqrt{1-\epsilon^2}\mu_0 I(r)/(2\pi r)$ where μ_0 is the vacuum permeability and $I(r)$ is the plasma current profile given as an input to the simulation. The magnetic field is characterized by a large toroidal component and a poloidal contribution as small as 10% of the total field strength. In addition, $R = R_0 + r\cos(\theta)$ with θ being the poloidal angle from the midplane. The $1/R$ dependence of the magnetic field results from the field strength inhomogeneity as the field is stronger near the center of the tokamak. The magnetic field remains constant in time which makes ELMFIRE an electrostatic PIC code.

The PIC method is well-established in plasma physics [25], and in ELMFIRE it is used to solve the gyrokinetic equations of motion. In this method, the plasma particles are simulated as numerical test particles each of which corresponds to billions of actual physical particles. This technique allows

efficient simulation of realistic, collective plasma behavior as it would not be possible to trace all the individual real particles present in the plasma. During a simulation, an ensemble of test particles is moved to follow real trajectories. The test particles are tracked as Lagrangian objects, which therefore can have any position in the continuous phase space. On the other hand, macroscopic plasma quantities are calculated as moments of the particle distribution function which is sampled at fixed three-dimensional grid points distributed equidistantly in the radial, poloidal, and toroidal directions.

The code simulates gyrokinetic ions and either drift-kinetic or adiabatic electrons. The gyrokinetic simulation is performed by tracing the path of the ion gyrocenters and representing the gyrating motion around the magnetic field lines with a gyroring that holds the charge of the particle. The Larmor radius of electrons is small compared to that of the ions because of their relatively small mass. In many cases, the electron Larmor radius is negligibly small compared to the plasma background scale lengths, and thus, it is more efficient, and yet accurate, to exclude the fast gyration of the electrons and represent their kinetics with a simplified drift-kinetic model instead. This method only simulates the motion of the particle gyrocenter. In the simulations performed in this thesis, the electrons are considered drift-kinetic. If the electron kinetics are not of interest, it is possible to simulate the ions together with an adiabatic electron response which is a further simplification. Modeling the electrons as adiabatic particles means that their contribution to the plasma is approximated by assuming that they follow a Boltzmann relation and respond to an electric potential through a simple analytic function.

The simulation is initialized by placing the plasma particles on the simulation grid corresponding to predetermined input profiles. First, ions are placed on integrated collisionless virtual orbits such that the required density profile is obtained. Second, electrons are placed on the gyrorings of the ions to ensure quasineutrality of the plasma. In the beginning of the simulation, a zero electric potential is assumed. The velocity of the particles is set to correspond to the local Maxwellian velocity distribution specified by a given user-defined temperature profile. In this work, the initial radial profiles for the temperature and density are defined as hyperbolic functions. The hyperbolic formula used for both the density and temperature radial profiles is

$$X = X_0 \left[1 + \alpha_X \tanh\left(\frac{r_0 - r}{\alpha_X L_X} \right) \right] \tag{4.2}$$

where the variable X corresponds to either density or temperature, $r_0 = (r_\mathrm{L} + r_\mathrm{R})/2$ with r_L and r_R being the radial limits of the simulation domain, and profile parameters X_0, α_X, and L_X are used for scaling and shaping the

profile. This profile initialization creates a tanh-shaped pedestal which has its steepest gradient located at the middle of the simulation domain.

As the simulation proceeds, the plasma particles are propagated along their gyrocenter orbits according to the equations of motion (appendix A). Following the particle movement, a charge separation forms and the resulting electric potential is solved. The newly obtained potential is considered as the particles are moved again to ensure quasineutrality of the plasma. Finally, the particles are collided using binary collisions between all the particle species. ELMFIRE uses a binary collision operator that utilizes a Monte Carlo based technique to pair test particles at random in collision cells and performs pairwise collisions [26, 27]. The collisions conserve energy, momentum and number of particles. Satisfying the conservation laws is required to correctly evolve the distribution function. The collisions are a stochastic process that scatter the individual particle velocities in an angle taken from a Gaussian distribution. A binary collision is effectively equivalent to a random walk in velocity space. In a plasma, the grazing Coulomb collisions only gradually change the velocity of a particle and large deflections occur as result of multiple small angle collisions.

The binary collision method enables neoclassical physics in the simulations, but additionally, ELMFIRE can incorporate turbulent features into the plasma. Purely neoclassical effects are obtained by flux surface averaging the charge separation between ions and electrons before solving the electric potential and advancing the particle gyrocenters in the simulation. The averaging does not allow instabilities to form in the potential. On the contrary, turbulence is included by letting the charge separation fully affect the electric potential and consequently develop turbulent fluctuations. Global gyrokinetic simulation codes, such as ELMFIRE, are used to accurately study micro-instability induced turbulence in a tokamak plasma [28]. ELMFIRE is able to reproduce the electrostatic micro-instabilities ITG and TEM. Capturing the complex, nonlinear turbulent fluctuations requires the turbulence simulations to use a dense spatial grid. The micro-instabilities have a characteristic scale length of the size of an ion Larmor radius and therefore the grid cells should have comparable size in the radial and poloidal directions. In addition, the electrons need to be simulated as drift-kinetic to capture their motion and the effects of the related instabilities. The fast electron motion in the parallel direction is the limiting factor for the time step used.

In this thesis, the focus is on the edge pedestal region, and therefore, it is sufficient to simulate a radial annulus of the torus without the magnetic axis. The simulations neither include the scrape-off layer (SOL) outside the last closed flux surface, although, in ELMFIRE there is an option to take the SOL into account. In ELMFIRE simulations, SOL dynamics have been

shown to enhance plasma transport near the plasma edge and slightly modify the temperature and density profiles [29, 30]. These effects from the SOL boundary model are, however, localized mainly at the edge region outside the plasma core, and thus, possibly largely outside the pedestal region. The simulation domain in this work is restricted to span radially from fixed r_{L} to r_{R} and boundary conditions are determined for the electrostatic potential at these radial limits. Either the potential or its gradient is defined to vanish at a boundary. In the simulations, the boundary conditions are chosen such that the electric potential is set to zero at the radial inner boundary of the domain and zero potential gradient is assumed at the radial outer boundary, which corresponds to zero radial electric field $E_r = -\partial\,\Phi/\partial\,r = 0$ V/m. Switching the boundary conditions for the electric potential did not have noticeable effect on the performed simulations. Additionally, particles leaving the plasma at the outer boundary are reinitialized back into the simulation domain as a pair of electron and ion at the end of each time step, and particles leaving at the inner boundary are reflected back in. The reinitialized particle pairs are returned to the plasma according to a prescribed ionization source profile. These boundary conditions were duplicated for all ELMFIRE runs.

Throughout the simulation ELMFIRE outputs several diagnostic macroscopic quantities as radial profiles, such as the density, temperature, and flow velocity. In practice, these quantities are sampled from the test particles at every time step and for each grid cell as weighted averages. From individual cells, the time evolving radial profiles are then computed by averaging over flux surfaces. The averaging is justified because the temperature and density of a tokamak plasma stay approximately constant within a magnetic flux surface. The parallel current density $j_\parallel$ is also outputted, from which the bootstrap current profile predicted by ELMFIRE can be determined. The code calculates the magnetic field weighted and flux surface averaged parallel current density as

$$\langle j_\parallel B\rangle = \sum_s Z_s e \langle n_s u_{\parallel,s} B\rangle \tag{4.3}$$

where $u_{\parallel,s}$ is the parallel flow velocity for species s. In the absence of a loop voltage there is no ohmic current present in the simulation and the entire $j_\parallel$ is comprised of the bootstrap current density with possibly contributions from turbulence and boundary effects.

Chapter 5

Simulation results

In this thesis, the bootstrap current profile predicted by ELMFIRE (v12c) simulations is studied in the steep edge pedestal tokamak plasma in the low-collisionality banana regime. The low-collisionality regime is typical for JET pedestal, and the bootstrap current has previously been studied with ELMFIRE in the collisional regime [31]. Results from neoclassical simulations are compared with two analytical models derived from neoclassical theory, and furthermore, the effect of turbulence is examined by allowing micro-instabilities to form into the simulated plasma. The computational resources were provided by CSC, IT Center for Science in Finland. During the work, CSC's supercomputer was upgraded from Sisu to Puhti, and the simulation code was ported to the new platform.

The simulation parameters corresponded to those present in the JET tokamak in a concentric limiter configuration. Thus, the parameters of the plasma equilibrium configuration were determined to be $a = 0.9357$ m for the plasma minor radius, $R_0 = 2.9056$ m for the tokamak major radius, and $B_t = 1.7$ T for the toroidal magnetic field strength. The annular segment simulated extended in radial direction from $r_{\mathrm{L}} = 0.77$ m to $r_{\mathrm{R}} = 0.93$ m, which in normalized radial coordinates corresponds to $r/a \approx 0.82-0.99$. This narrow region contains the pedestal region inside the last closed flux surface. The performed analyses used pure plasma containing only the main ions and electrons. The main ion species corresponded to deuterium with charge number $Z_i = 1$ and mass $m_i = 2.014$ u with u being the atomic mass unit.

Some approximations were made regarding the simulations in comparison to actual experiments. JET does not have a circular cross section which ELMFIRE uses in the simulations but rather a vertically elongated one with triangularity. In addition, the SOL is not simulated. Therefore, the predictions are not equivalent to measurements. Also, simulating an entire experimental plasma discharge is not possible in practice due to computational

limitations. However, short time scale phenomena arising during the first few ion collision times are studied.

5.1 Implementation of the Hager model

Comparing a numerical code against analytical formulas serves to verify that the code performs as intended [32]. In this thesis, the neoclassical Sauter model together with the Hager model are used for the verification. In addition, the intent was to evaluate whether one of the two models better describes the converged simulation results of the equilibrium bootstrap current density profile in the studied regime. As part of its diagnostics, ELMFIRE calculates and outputs the bootstrap current density according to the Sauter formula of equation (3.1). As part of this thesis, the Hager formula was implemented into the code as in equation (3.2).

These analytical estimates for j_{bs} are calculated using the plasma profiles obtained from the simulation. The profiles used for the density and temperature mimic a JET equilibrium with a steep pedestal. The shapes of these profiles were initialized with hyperbolic tangent functions to fit the large gradients that correspond to given gradient scale lengths $L_{n,T} = 0.06$ m (Fig. 5.1). The scale length value refers to the steepest gradient located in the middle of the simulation domain.

The scenario with the described plasma profiles is considered the base case in which the Hager model agrees within 5% with the Sauter model (Fig. 5.2 (a)). The Hager model predicts larger j_{bs} and the largest relative

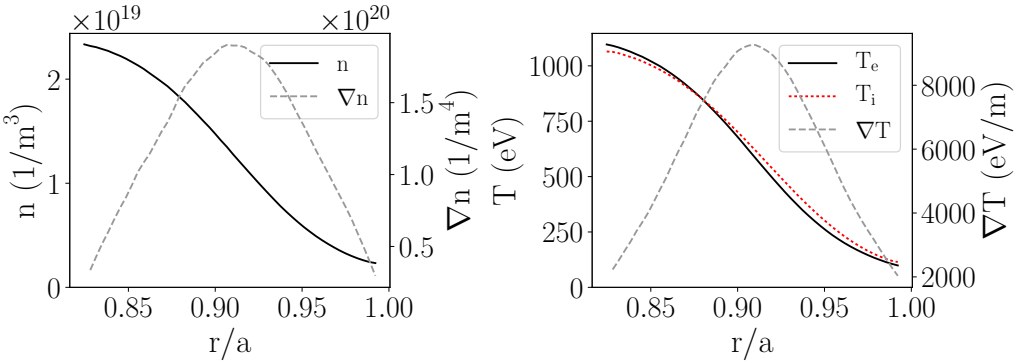

Figure 5.1: Radial density n and temperature T profiles (left axis) and their gradients (right axis). The profiles are initialized with gradients corresponding to $L_{n,T} = 0.06$ m. The ion and electron densities are assumed the same due to quasineutrality.

difference between the two analytical models is observed at the location of the maximum current density value at $r/a \approx 0.89$. A similar behavior was also previously observed in the banana regime where the Sauter model is reported to underestimate the bootstrap current [20]. The simulation was performed without considering effects from the Shafranov shift. It should be noted that the circular geometry used by ELMFIRE is unshifted, and therefore, the damping term $\beta_{\nabla T_i}$ of the Hager model, which otherwise would incorporate the Shafranov shift into equation (3.2), was ignored.

The bootstrap current in the pedestal region has a peaked current density

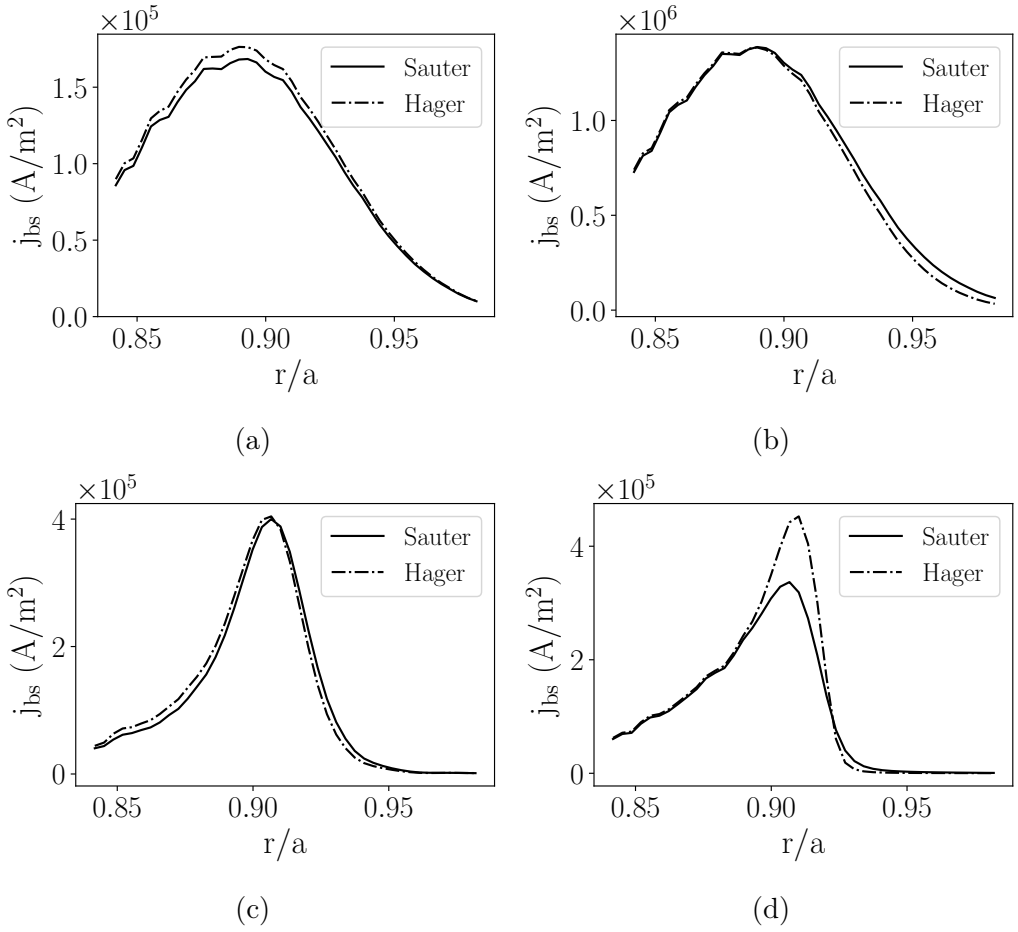

Figure 5.2: Comparison of the Hager model to the Sauter model. The radial profiles used for calculating j_{bs} were collected from four different ELMFIRE simulation cases which are (a) the base case, (b) increased collisionality with increased density, (c) increased density gradient, and (d) increased temperature gradient.

profile. The shape results from the dependence of j_{bs} on the radial density and temperature gradients located at the pedestal, which in this case are defined the largest in the middle of the domain at $r/a \approx 0.91$ (Fig. 5.1). In addition, the bootstrap current is stronger at lower collisionality. Since the collisionality varies across the steep pedestal decreasing toward the plasma center, the maximum value of j_{bs} is located radially inward from the largest gradients. The significant ν_* produced near the outer boundary prevents complete banana orbits and consequently the bootstrap current is reduced drastically in this region. The peak current location is typically between the maximum gradient and the top of the pedestal, which was also observed for the base case.

In an effort to assess the changes included in the Hager formula compared to that by Sauter through the various correction terms, the plasma profiles were modified. First, the particle density was increased tenfold in order to increase the collisionality of the plasma (Fig. 5.2 (b)). The Hager formula is expected to be more accurate than the Sauter formula at higher electron collisionality ν_{e*}. The increased collisionality reduces j_{bs} estimated by the Hager model relative to the estimate by Sauter in comparison to the base case throughout the simulation domain. The two models agree at the location of the maximum current density but some discrepancy is observed near the outer boundary where the Hager formula predicts lower current density. From the middle of the simulation domain toward the outer boundary the plasma is no longer in the banana regime but corresponds to the plateau regime. Because j_{bs} is decreased in magnitude when moving away from the center of the plasma, the relative difference between the models has increased to around 48% near the edge at $r/a \approx 0.98$. The Sauter model has been described to overestimate the bootstrap current for large collisionality [20, 21] which is consistent with the result observed here. It is worth noting that j_{bs} has increased by nearly an order of magnitude compared to the base case as a result of the increased particle density.

Second, the increase in the plasma pressure gradient was studied by steepening both the temperature and density gradients in the middle of the domain one at a time (Fig. 5.2 (c) and (d)). The density and temperature profiles are initialized in these cases with gradient scale lengths $L_{n,T} = 0.01$ m. The short scale lengths highlight how the models are affected by a steep pedestal, however, the exact values chosen may actually be already too short in actual JET experiments where n_e and T_e pedestal widths are between 2 – 3 cm [33]. The Sauter formula is intended for modeling plasmas that satisfy the locality approximation while the Hager model is implemented specifically with the pedestal conditions in mind, where the ion banana orbit width becomes comparable to the pressure gradient scale length. The steeper

profiles provide stronger current drive, and thus, the magnitude of j_{bs} is observed to be increased compared to the base case. In addition, the large gradients have such a considerable effect on the bootstrap current that the current density profile is peaking in both cases at the location of the steepest gradients at $r/a \approx 0.91$. As the plasma density gradient is increased, the models estimate very similar profiles, the relative difference at the peak current location is only 1%. In turn, when the temperature gradient is increased, the Hager model shows a significant deviation from the Sauter model. The relative difference in the current density in comparison to the estimate by Sauter at the peak current location is around 42%.

Even though ELMFIRE will not be able to account for the Shafranov shift, the effect of the shift on the bootstrap current density estimated by the Hager model was examined to quantify the difference it makes in comparison to the Sauter model. In the base case with low collisionality, the observed change was insignificant although j_{bs} was reduced in the entire simulated region (Fig. 5.3). At the location of the maximum current density at $r/a \approx 0.89$ the decrease in j_{bs} was around 5% as the Hager model decreased on the same level as the Sauter model when the shift was increased all the way to $\Delta_R = 0.5$. Therefore, the density of the plasma was increased in a separate ELMFIRE run, making the simulation correspond to the case shown in Fig. 5.2 (b).

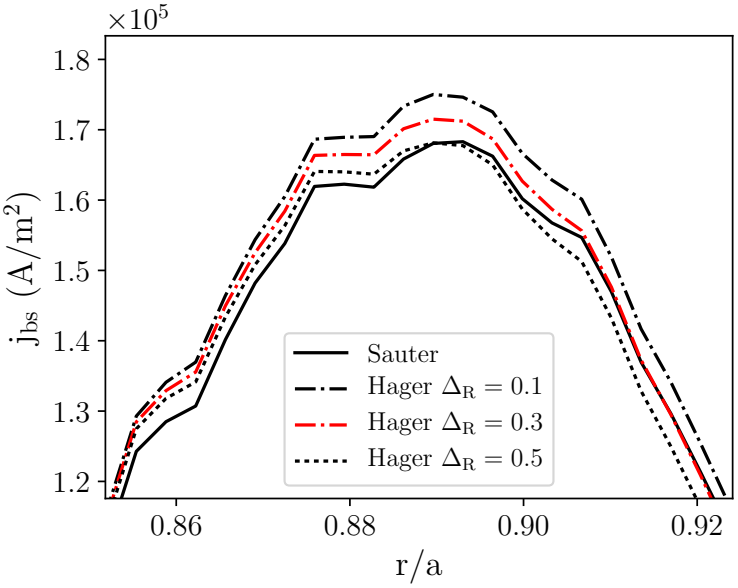

Figure 5.3: Effect of Shafranov shift Δ_R on the radial j_{bs} profile around the maximum current density location in the base case.

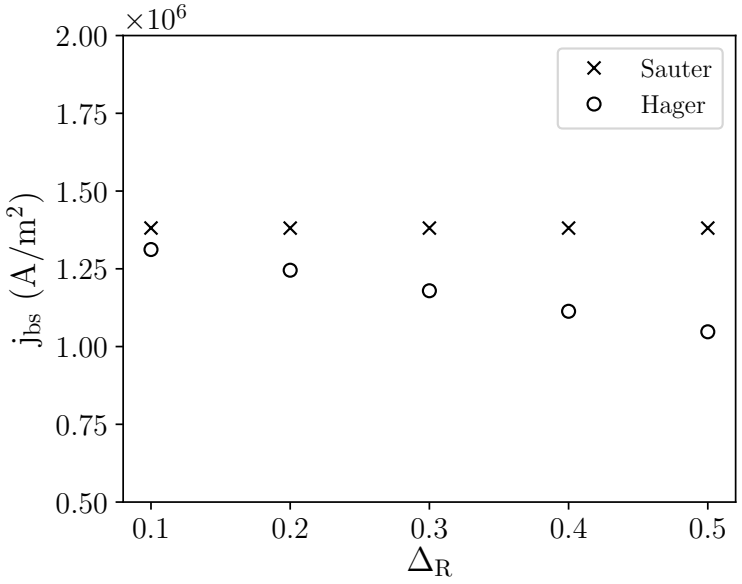

Figure 5.4: Scan of j_{bs} as a function of the Shafranov shift Δ_R. The j_{bs} values are collected from the maximum current density location. Particle density has been increased by an order of magnitude compared to the base case to increase collisionality.

This situation is similar to the conditions for which Hager et al. [21] reported large differences between the models as the collisionality starts to play a role. In this case, having the Shafranov shift included in the Hager model was observed to decrease the magnitude of the estimated j_{bs} more significantly and result in a clear deviation between the two models (Fig. 5.4). Larger shift leads to larger discrepancy in the performed Shafranov shift scan. The j_{bs} values predicted by the Hager model decrease linearly as a function of the Shafranov shift, and the relative difference to the prediction by Sauter ranges from 5% to 24% when the shift is increased from $\Delta_R = 0.1$ to 0.5.

Steeper gradients in both the density and temperature profiles enhance the magnitude of the bootstrap current density and they also further increase the difference in the predictions by the two models as shown in the gradient scale length scans with Shafranov shift (Fig. 5.5). When the gradient scale lengths become shorter and get closer to the size of the ion banana orbit width, the Hager model reduces the bootstrap current density more significantly than the Sauter model. The term in the Hager model that includes the Shafranov shift is a damping term that is designed to take into account the finite ion orbit width effects particularly in the presence of a steep ion temperature

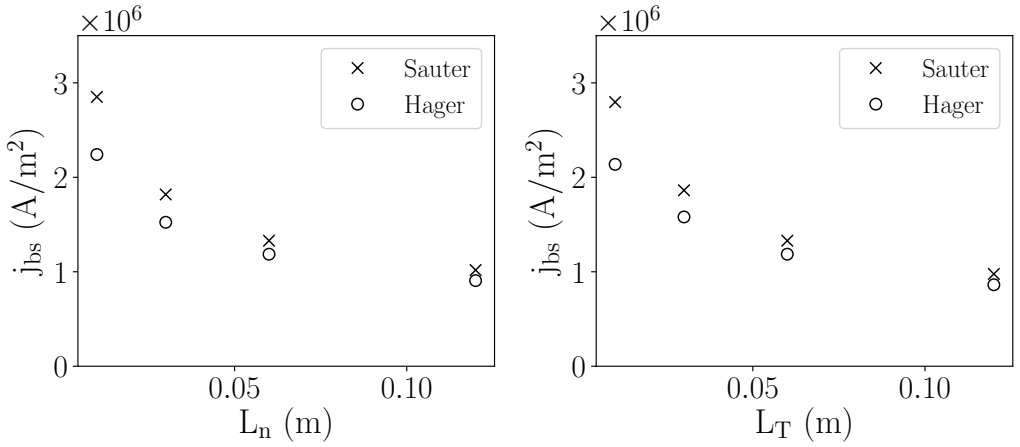

Figure 5.5: Scan of j_{bs} as a function of the gradient scale lengths for (a) density, L_n, and (b) temperature, L_T. The j_{bs} values are collected from the maximum current density location. Shafranov shift is set to $\Delta_R = 0.3$ and particle density has been increased by an order of magnitude compared to the base case.

gradient, which explains the observed behavior at the edge pedestal. The Hager formula in its full form with finite Shafranov shift included and with higher collisionality predicts consistently lower current density than the Sauter formula in the pedestal.

5.2 Neoclassical simulations

ELMFIRE solves the parallel plasma current from the simulated particle flow. This parallel current specifically represents the bootstrap current when the loop voltage and, consequently, ohmic current are omitted from the simulation. The neoclassical bootstrap current density is studied by suppressing turbulence and allowing the current density profile to develop and evolve purely according to neoclassical physics. The neoclassical simulation results of this work were compared to estimates by analytical neoclassical models from both Sauter and Hager.

The simulations used a grid with $50 \times 50 \times 8$ cells in the radial, poloidal, and toroidal directions, respectively. The exact grid resolution, however, is not critical in the neoclassical simulations with flux surface averaging. The grid cells have equal size in the radial direction, and per each radial

location the cells are uniformly spaced in the poloidal and toroidal directions. The total number of particles used corresponded to 2890 particles per cell on average. The binary collision grid had size 300×300 with the collision cells corresponding to the radial and poloidal directions. The ELMFIRE simulations were performed with drift-kinetic electrons that define the shortest time step required for accurate simulation. Because of the small mass of the electrons, their thermal speed along the helical magnetic field lines is considerably faster than that of the ions. The time step used is determined such that there are sufficient number of steps included along the torus to achieve $\Delta t \leq \Delta z / v_{\mathrm{th},e}$ where Δz is the grid cell size along the field. The time step used in the neoclassical simulations was $\Delta t = 50$ ns while the smallest $\Delta z / v_{\mathrm{th},e}$ in the simulation domain was 116 ns at the inner boundary where the temperature is the largest.

Numerical plasma particle simulations are very time consuming due to the short time step required and the large grid with a massive amount of particles needed to reduce statistical noise. In an effort to obtain converged simulations to reach the neoclassical equilibrium in reasonable time, the particle density of the simulated plasma was multiplied by five compared to the original base case introduced in the previous section 5.1. The temperature was not modified and the profiles were initialized to the tanh-shaped pedestals, similar to the ones shown in Fig. 5.1. The higher density increases the ion collision frequency and collisionality of the plasma, and consequently drops the ion collision time accordingly which is the reason for quicker convergence. Regardless, it was ensured that the particles stay mainly in the banana collisionality regime as intended. This higher density scenario is used as the base case for the neoclassical bootstrap current study.

The ELMFIRE predicted bootstrap current density converges after a simulation time corresponding to approximately one ion collision time. Fig. 5.6 shows the convergence of j_{bs} predicted by ELMFIRE together with the analytical estimates in the pedestal. The ion collision time τ_i used for time normalization is considered locally and it is calculated from the initial plasma density and temperature profiles. The initial transitory phase in the start of the simulation is clearly visible in the figure. The simulation essentially goes through a numerical transient when the system is initialized in an equilibrium during which the macroscopic quantities can change quite remarkably before settling. After reaching equilibrium, the j_{bs} profile evolves slowly according to physical transport. However, the simulated j_{bs} is seen to oscillate strongly in time even after converging. These noisy temporal oscillations result from the electron contribution to the current density. Therefore, to obtain a single characterizing value for a given radial location, the current density is time averaged. To reliably evaluate the converged j_{bs} without the initial transient

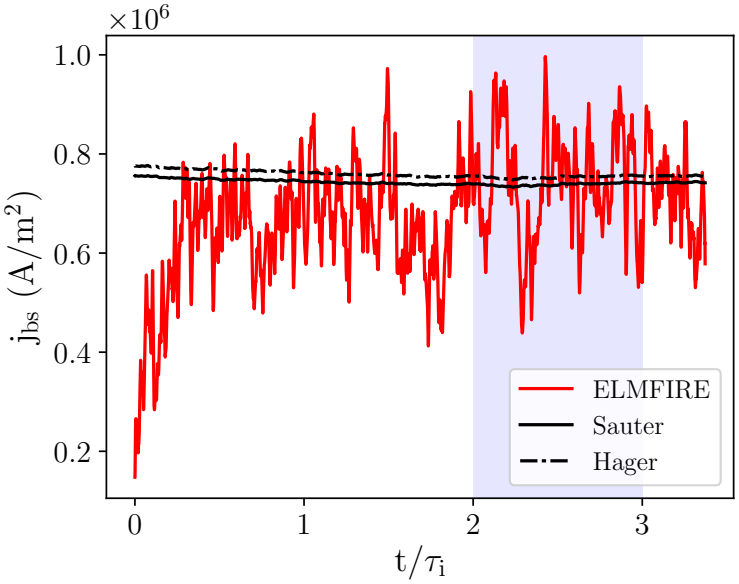

Figure 5.6: Time evolution of the bootstrap current density at the peak current location at $r/a \approx 0.89$. The j_{bs} simulated with ELMFIRE is compared to the analytical estimates by Sauter and Hager as a function of normalized time where $\tau_i \approx 330$ μs. The shaded area illustrates the time window over which the simulation result for the radial location is averaged.

plasma state affecting the calculation, the time window used in the averaging is taken to cover the time $2-3\tau_i$ for the peak current location parameters.

The bootstrap current density profile predicted by ELMFIRE converges to the analytical estimates in the simulated edge pedestal region. However, some discrepancy is observed toward the center of the plasma where the simulation predicts lower j_{bs} (Fig. 5.7). This disparity near the inner boundary likely results from boundary effects and was observed also previously in ELMFIRE simulations [31]. Otherwise, the simulated j_{bs} in the neoclassical equilibrium is within numerical precision equal to the analytical estimates showing quantitative agreement with theory. The analytical formulas give very similar results with only a small difference of around 2% between each other at the peak current location at $r/a \approx 0.89$. The Hager model estimates higher current density than the Sauter model. The electrons carry most of the bootstrap current, the ion contribution to j_{bs} is small in comparison but not negligible. The ions contribute around 24% of the total current density at the maximum current density location.

Locality of the plasma transport required by the neoclassical theory

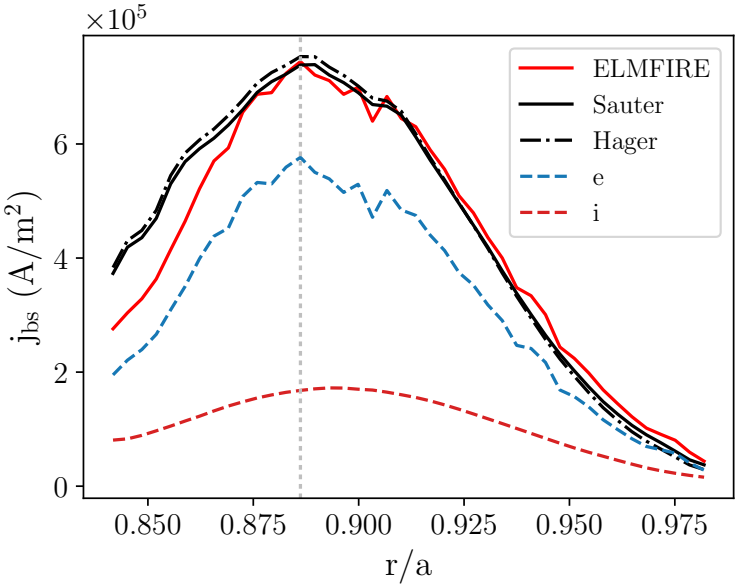

Figure 5.7: Radial bootstrap current density profile showing the ELMFIRE simulation result and the analytical estimates by Sauter and Hager. The simulated j_{bs} consists of electron (e) and ion (i) contributions. The dashed vertical line indicates the location of the maximum bootstrap current density at $r/a \approx 0.89$.

is verified by studying the non-locality parameters. For the density and temperature these parameters $\rho_p/L_{n,T}$ stay below 0.3 over the entire domain which ensures that the models operate within the neoclassical limits and that the neoclassical approximations are valid (Fig. 5.8). At the peak of the current density profile, the values are $\rho_p/L_n \approx 0.20$ and $\rho_p/L_T \approx 0.17$. Additionally, the neoclassical base case simulation remains in the banana regime $\nu_{i*} < 1$ over most of the simulation domain. The ion collisionality can be observed to increase when approaching the outer boundary but it grows above unity only near the edge around radial location $r/a \approx 0.96$. At the maximum j_{bs} location, the ion collisionality ν_{i*} is 0.34 and the electron collisionality ν_{e*} is 0.43.

5.2.1 Collision cell scan

Previously, the accuracy of the Monte Carlo binary collision model used in this thesis has been studied with respect to simulation time step [34, 35] and with respect to the number of test particles simulated per collision cell [34].

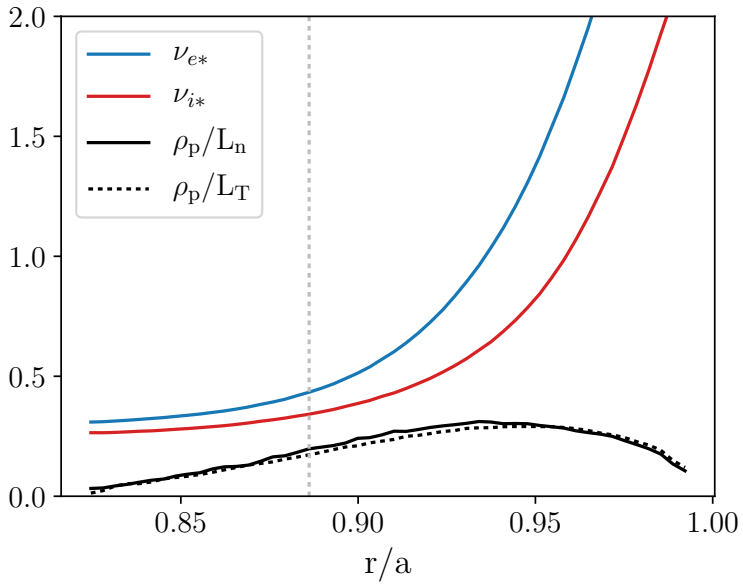

Figure 5.8: Radial profiles of collisionality and locality over the simulation domain. The dashed vertical line indicates the location of the maximum bootstrap current density.

The collision model was demonstrated to convergence close to an accurate solution with 400 particles per cell as long as the time step used is sufficiently small. Here, the effect of collision grid density is investigated.

ELMFIRE uses a Monte Carlo particle collision scheme in which the simulated test particles are paired and collided in a number of binary collision cells. The simulations take the specific number of pairing slots as a user-defined input. To study the effect of the number of collision cells used on the simulation accuracy and the numerical precision of the results, their number was varied in a scan (Fig. 5.9). The scan included collision grids with sizes $N_{\mathrm{cells}} = N \times N$ defined using $N = 30,\ 100,\ 200,\ 300,\ 450$. The simulation domain was thus partitioned in N uniformly distributed collision cells in both radial and poloidal directions. The total number of particles was kept fixed between simulations. One should note that the number of particles per collision cell changes. Even for the case $N = 450$ the number of particles per cell is approximately 300 on average, which is sufficiently high for particle number convergence [34]. Hence, it was tested whether changing only the collision cell size would affect the result without having to simulate more particles. Typically, increasing the number of particles improves the accuracy of PIC codes and reduces statistical noise but, as a penalty, it increases

simulation time.

Increasing the number of binary collision cells was observed to improve the quantitative agreement between the converged ELMFIRE simulation result and the analytical estimates by Sauter and Hager (Fig. 5.9). With 300×300 collision cells, corresponding to the neoclassical base case, the simulated mean bootstrap current density is within 3% from both theoretical predictions. Adding more collision cells did not notably enhance the result, but with fewer cells, ELMFIRE predicts distinctly lower j_{bs} values. The two cases with the sparsest grids remain well below their corresponding analytical estimates, the relative difference for both is around 20%. The simulated j_{bs} experiences strong temporal fluctuations (Fig. 5.6), which produces significant uncertainties. The error bars in Fig. 5.9 illustrate one standard deviation form the mean and their size does not change when the number of collision cells is altered. Additionally, no improvement in the j_{bs} profile predicted by ELMFIRE near the inner boundary of the simulation domain was observed. The same discrepancy as in Fig. 5.7 is observed in all cases. Furthermore, increase in N_{cells} did not have considerable effect on simulation time.

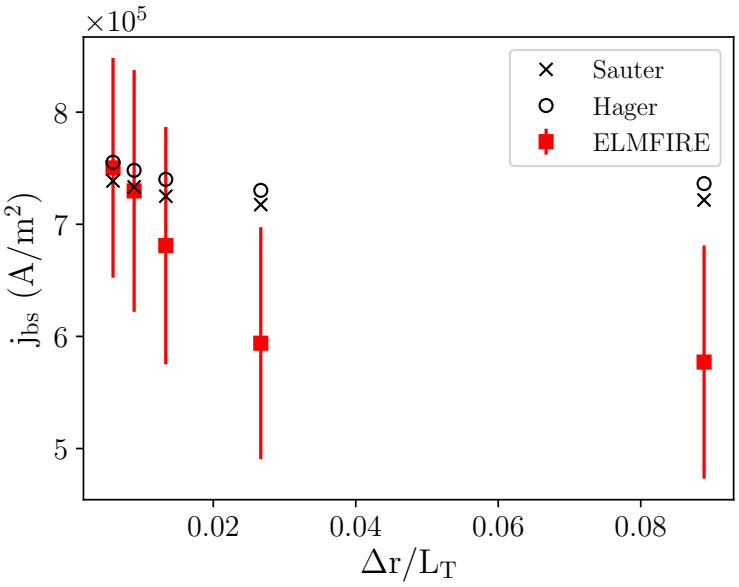

Figure 5.9: Scan of j_{bs} as a function of normalized binary collision cell size, $\Delta r/L_T$. The j_{bs} values are collected from the maximum current density location, and the error bars represent one standard deviation around the mean value. Δr is the collision cell width in the radial direction and $L_T = 0.06$ m is the temperature gradient scale length in the middle of the pedestal.

The test particles are paired for collisions from finite sized neighborhoods, the extent of which is determined by the number of collision cells used. The denser the grid is, the smaller is the volume one cell covers. The binary collision operator used by ELMFIRE assumes that the plasma background properties stay similar within each of these collision cells. Most importantly the background density and temperature cannot vary substantially. During a simulation, the particle density is sampled to the simulation grid, and thus, the density considered in the collisions is fixed in each of the spatial grid cells. The smallest studied collision grid had size 30×30 which is sparser than the 50×50 grid describing the density background in the radial and poloidal directions, violating the assumption for the collision operator. For the larger collision grids tested in the scan, the resolution for the density is no longer a limiting factor, but accurate enough temperature resolution is also required.

The plasma temperature profile determines the speeds of individual particles. In particular, across a steep pedestal, the temperature changes abruptly and so do the velocities of the particles in that region. When particles collide, their relative velocity is scattered and new velocities for both particles are calculated from the result. The collision process inevitably introduces non-locality in the updated particle velocities because the colliding particles are paired at random within a collision cell. The random pairing is an approximation compared to true collisions but is often considered sufficient in simulation. However, depending on the used grid size, the particles can have significant distance between each other. The differences observed between the studied simulation cases could result from the introduced inaccuracy in individual particle velocities and in their evolution. The speed of the particles relate to temperature through the equation for $v_{\mathrm{th}} = \sqrt{2T/m}$, and the change of average temperature within a collision cell with radial width Δr can be approximated by $\Delta r \nabla T = \Delta r T / L_T = (\Delta r / L_T) T$. Inside a cell of the sparsest studied collision grid, the difference in temperature $\Delta r / L_T$ can be around 10% when $L_T = 0.06$ m which at the very high temperatures involved becomes significant. With the grid size 300×300, the difference is already less than 1%. Estimating bootstrap current numerically requires accurate modeling of parallel flow velocity, and in the ELMFIRE simulations, the average parallel velocity of a particle species is sampled from the individual particle velocities which allows small inaccuracies to accumulate. Therefore, more accurate description of the velocity distribution obtained with denser collision grids is likely improving the simulated j_{bs}. Curiously, when large deviations are observed from analytical estimates, the numerical j_{bs} values are in all cases predicted lower in magnitude.

5.2.2 Scale length scan

The agreement of the numerical simulation with theory in the neoclassical limit was tested in separate scans of the gradient scale lengths. Neoclassical methods assume that the plasma properties stay approximately unchanged within the width of an ion banana orbit. However, when the profile gradients are steep, which is often the case in pedestal region, the validity of the analytical formulas may start to break. The gradient scale lengths of density and temperature were varied in the scans one at a time by modifying the gradients of the initialized profiles in the middle of the simulation domain. The scale lengths used were $L_{n,T} = 0.01$ m, 0.03 m, 0.06 m, and 0.12 m. At the same time, the poloidal ion Larmor radius estimating the ion orbit width was kept fixed, $\rho_p \approx 0.017$ m, at the same location in the middle of the pedestal, $r/a \approx 0.91$. However, ρ_p experiences small changes closer to the boundaries when the temperature profile is altered. At the boundaries, the gradients are more gentle due to the shape of the hyperbolic tangent profiles so the strongest effect on the non-locality parameters is still achieved around the middle of the domain.

The bootstrap current density j_{bs} predicted by ELMFIRE using the modified density and temperature scale lengths $L_{n,T}$ agrees quantitatively

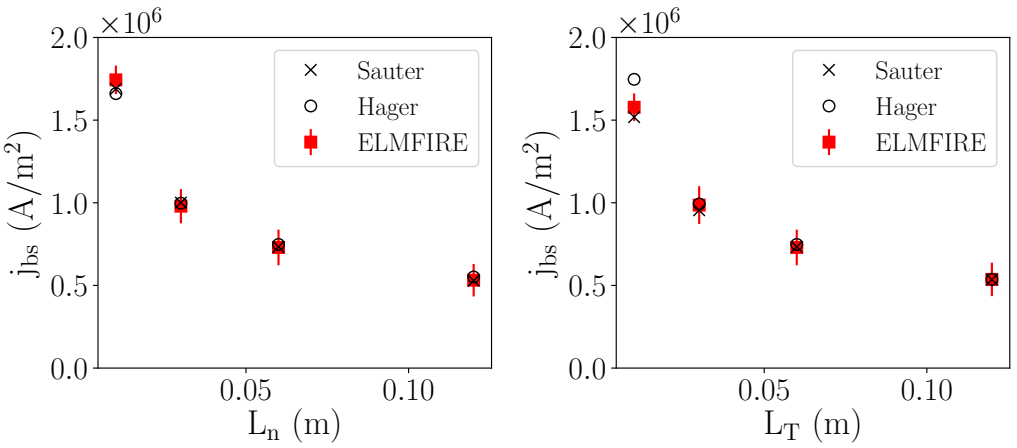

Figure 5.10: Scan of j_{bs} as a function of the gradient scale lengths for (a) density, L_n, and (b) temperature, L_T. The j_{bs} values are collected from the maximum current density location, and the error bars represent one standard deviation around the mean value. The neoclassical base case simulation has $L_{n,T} = 0.06$ m.

with the estimates from theory when the predictions are compared to the analytical models by Sauter and Hager (Fig. 5.10). Within the numerical accuracy of ELMFIRE the simulated j_{bs} matches the two different analytical estimates. Generally, when the approximations from neoclassical theory are no longer applicable, plasma simulation codes can still provide accurate results. The Hager formula was also meant to have improved accuracy in these conditions compared to the Sauter formula. However, in this case, no remarkable differences are observed, and both models predict very similar results in the banana regime. Based on the results in section 5.1, differences are expected to arise between the models if effects from the Shafranov shift were included in the study and we were operating in more collisional regime. However, the Shafranov shift would then need to be implemented in ELMFIRE to observe if the predictions better correspond to one model over the other.

The shortest scale lengths considered, $L_{n,T} = 0.01$ m, are of the order of an ion orbit width which breaks the small orbit width approximation. The corresponding non-locality parameters violate the required condition $\rho_p/L_{n,T} \ll 1$. Gradient scale lengths this short are likely artificial and may not be encountered in actual JET experiments [33]. The shortest temperature gradient scale length was also discovered problematic to simulate with ELMFIRE because the plasma background profiles began to evolve strongly early in the simulation, and the current density j_{bs} did not have enough time to fully converge. Therefore, the prediction for the case $L_T = 0.01$ m is considered potentially incomplete.

5.3 Turbulence simulations

Micro-instability driven turbulence drives current in the tokamak, and the turbulent contributions produce deviations from neoclassical predictions. Therefore, to investigate the effect of turbulence on the bootstrap current, a plasma with both neoclassical transport and electrostatic turbulent fluctuations present was examined. The parallel plasma current from ELMFIRE turbulence simulations, which can include both the conventional bootstrap current and its turbulent analogue, is compared to the analytical models by Sauter and Hager to investigate the difference to neoclassical theory. Both ITG mode and TEM driven turbulence were considered.

The neoclassical base case simulation had to be modified for the simulation of turbulent transport. To be able to resolve the turbulent features resulting from electrostatic plasma instabilities, the spatial simulation grid of high spatial resolution was set up. The grid cell size in the poloidal plane needs to be comparable to the ion Larmor radius which is the characteristic scale of

the turbulence. Even with the relatively narrow annulus shaped simulation domain used in this work, the poloidal dimension is rather extensive with the JET parameters and it necessitates a large number of grid cells in the corresponding direction. Thus, the toroidal magnetic field strength was lowered to $B_t = 1.2$ T in order to increase the ion Larmor radius to a level that would allow for a computationally feasible grid density. The ion Larmor radius was in this case $\rho_i \approx 0.004$ m in the middle of the pedestal, which corresponds to approximately 1440 poloidal grid cells. The radial and toroidal resolution from the previous neoclassical runs were sufficient also for the turbulent case.

However, the turbulence simulation did not converge when the high grid resolution was used, and numerical issues were observed right in the initial phase of the simulation. The temperature of the particles started to rise, especially the electron temperature near the inner boundary, and consequently, the electron parallel flow velocity was strongly influenced because the increase in temperature increases the particle velocities. Increased particle velocities need to be taken into account in the simulation time step but decreasing the time step to half from the original value to $\Delta t = 25$ ns did not improve the convergence of the simulation. The change in the temperature was so substantial that the difference between the simulated plasma current and the analytical estimates became orders of magnitude larger than previously observed in the neoclassical study. The reason for the observed behavior near the domain boundary while simulating turbulence may be the boundary conditions set for the particles. It is possible that the reflective boundary condition at the inner boundary does not adequately conserve energy, and with the turbulent fluctuations pushing relatively large amount of particles out of the domain during simulation and a large number of reflections occurring, the inaccuracy in the energy of the system accumulates. This is then seen as a large, unphysical temperature increase.

A smaller number of grid cells was observed to enhance the performance of the simulation and allow the prediction to reach convergence at least in parts of the domain. Here, a similar spatial grid was used as in Ref. [36] in another turbulence simulation with the ELMFIRE code in the low collisionality regime. The simulation grid was defined with $50 \times 210 \times 8$ cells in the radial, poloidal, and toroidal directions, respectively. The toroidal magnetic field strength was kept at the previously determined low value of $B_t = 1.2$ T and the total number of particles simulated was increased from the neoclassical study to correspond to approximately 6200 particles per cell on average. The edge pedestal plasma profiles were modified to correspond to the desired dominating instability.

5.3.1 Impact of ITG turbulence on j_{bs}

To make ITG the dominating instability for the studied parameters, the plasma profile gradients were initialized with scale lengths $L_n = 0.12$ m and $L_T = 0.03$ m. Hence, the steep ion temperature gradient functions as a drive for the turbulence at the pedestal. The bootstrap current density profile from the turbulent simulation is observed to converge close to the analytical Hager model estimate near the edge where the collisionality is the largest. Closer to the center of the simulation domain, however, where j_{bs} peaks, the magnitude of the prediction does not reach the neoclassical estimates and remains well below both Sauter and Hager (Fig. 5.11). The numerical issues of the simulation in the studied parameter regime are still present near the inner boundary and they are found to strongly affect the j_{bs} profile quite far into the domain. These boundary effects lead to a large discrepancy between the numerical and analytical results.

With turbulence enabled in the simulation, the plasma profiles change more notably in time than previously observed with the neoclassical case in section 5.2 due to profile relaxation. The altered profiles modify the analytical bootstrap current predictions as well (Fig. 5.12). The particle and energy transport are increased in the pedestal plasma compared to the neoclassical

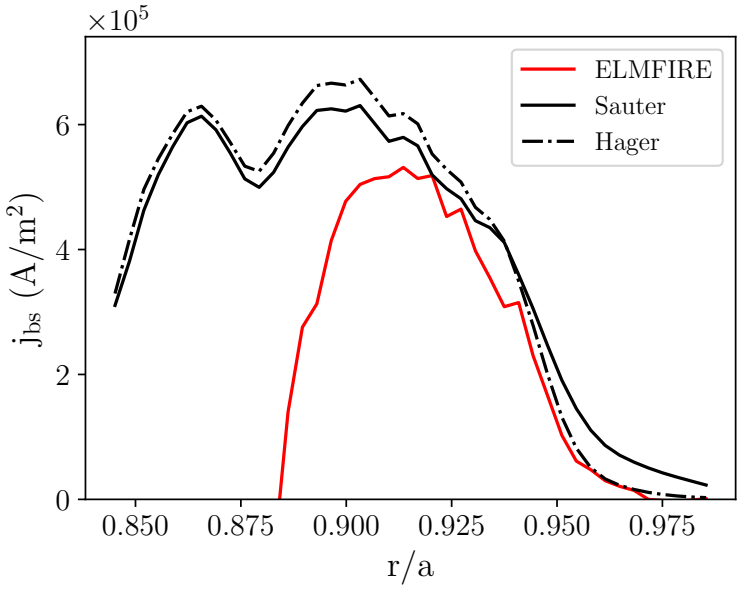

Figure 5.11: Radial bootstrap current density profile with ITG mode dominated turbulence included showing the ELMFIRE simulation result and the analytical estimates by Sauter and Hager.

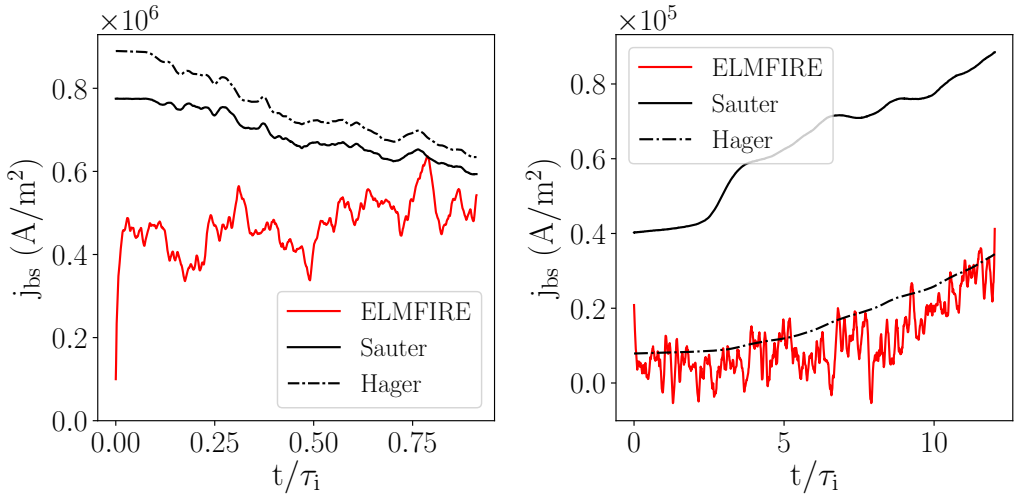

(a) (b)

Figure 5.12: Time evolution of the bootstrap current density with ITG mode dominated turbulence included (a) at the middle of the pedestal at $r/a \approx 0.91$ where $\tau_i \approx 340$ μs and (b) near the edge at $r/a \approx 0.96$ where $\tau_i \approx 30$ μs. The j_{bs} simulated with ELMFIRE is compared to the analytical estimates by Sauter and Hager as a function of normalized time.

case when the ITG mode is unstable. The analytical estimates for j_{bs} at the middle of the pedestal are observed to decrease as they adjust together with the evolving pedestal profiles (Fig. 5.12 (a)). At the same time, the bootstrap current density predicted by ELMFIRE remains $10-20\%$ below the analytical models. Most likely the simulation time is not long enough because the simulation has had only less than one ion collision time τ_i to evolve due to computational limitations. A typical simulation in the turbulent case ran on the Puhti supercomputer with 600 CPU cores for three consecutive days. This simulation time corresponds to over 6000 time steps which at the middle of the simulation domain equals $0.9\tau_i$. Unfortunately, the option to continue the simulation from a checkpoint file did not work on Puhti which was a major computational restriction. On the other hand, near the edge where the collisionality is higher and the plasma corresponds to the plateau regime, the simulation has had time to experience multiple ion collision times and the ELMFIRE simulation converged during this time better to the estimate by Hager (Fig. 5.12 (b)). In the initial phase of the simulation when only a few ion collision times have passed, however, the prediction from the simulation is only around 50% of the Hager estimate also at the region near the outer boundary. The better convergence is observed after around $10\tau_i$ have passed.

These results suggest that a longer simulation is needed to get a physically more appropriate result near the middle of the pedestal as well.

In the middle of the pedestal where the gradients are the steepest, $r/a \approx 0.91$, the turbulent fluctuation amplitude in the numerical simulation was $|e\delta\Phi/T_e| \approx 0.06$ which implies that significant deviations from a neoclassical current profile can be expected [22]. According to the study by McDevitt et al. [10], even small fluctuations with amplitude of only a couple percent are sufficient to produce a clearly noticeable contribution from turbulence to the parallel electron current. From equation (3.3) it is observed how the fluctuation amplitude affects the relative diffusion strength by turbulent transport, and thus, the simulation result is expected to have a large contribution from turbulence. Furthermore, the ion heat transport coefficient χ_i has increased during the simulation to oscillate between $3-4$ m^2/s in contrast to the coefficient staying on average below 0.5 m^2/s in the neoclassical study, further verifying the strong influence from turbulent fluctuations on transport. The large differences from the neoclassical predictions observed in the j_{bs} profile could partially be explained by the strong turbulence.

5.3.2 Impact of TEM turbulence on j_{bs}

A steep density gradient makes TEM the dominating instability, and accordingly, the plasma profile gradients were next initialized with gradient scale lengths $L_n = 0.06$ m and $L_T = 0.12$ m. Additionally, the density of the plasma was increased by a factor of two compared to the ITG and neoclassical simulation cases to increase the collisionality which would allow for more ion collision times to be simulated. The gentle temperature gradient defined makes the collisionality over the domain also more uniform. While operating in the banana regime in all of the simulation domain, the collisionality was now higher, $\nu_{i*} \approx 0.62$, in the middle of the domain. Because the grid resolution in the poloidal direction is not comparable to the characteristic length scale of the turbulent mode in the turbulence simulation, the simulation cannot resolve all the shortest length scales and they get filtered. The effect is more pronounced for the TEM than the ITG instability. This will reduce the accuracy of the turbulence simulation and possibly cause some dissipation of the turbulent fluctuations.

The numerical bootstrap current density predicted by ELMFIRE is observed to reach a distinctly lower magnitude than the analytical estimates from neoclassical theory almost throughout the simulated pedestal region (Fig. 5.13). Only near the edge, the ELMFIRE prediction is seen to converge to the analytical estimates by Sauter and Hager, both of which estimate very much the same profile. However, the relative difference between ELMFIRE and

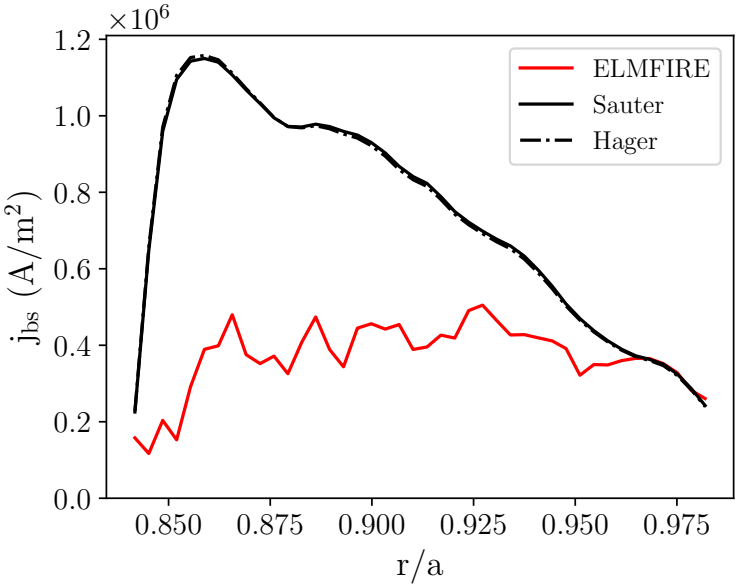

Figure 5.13: Radial bootstrap current density profile with TEM dominated turbulence included showing the ELMFIRE simulation result and the analytical estimates by Sauter and Hager.

the neoclassical theory in the middle of the pedestal at $r/a \approx 0.91$ is already 40%, and it increases toward the center of the plasma. In comparison to the ITG case, the discrepancy is not as significant at the inner boundary, and the simulated j_{bs} stays directed toward the positive direction. The negative boundary effects do not affect the simulation as drastically as in the ITG case which may be consequence from the higher collisionality.

The time evolution of the bootstrap current density shows similar behavior as observed before with the ITG simulation case (Fig. 5.14). At the middle of the pedestal, the magnitude of the j_{bs} predicted by ELMFIRE does not reach the level of the analytical estimates and the difference remains large over the period of two ion collision times τ_i simulated (Fig. 5.14 (a)). Similar simulation time was sufficient for converging the ELMFIRE prediction previously with the neoclassical simulations in section 5.2. As in the ITG case, the match is better at the region near the outer boundary, where the numerical j_{bs} already quite well corresponds to the analytical estimates at $1.5\tau_i$ (Fig. 5.14 (b)). A longer simulation would offer a confirmation whether the difference in the bootstrap current remains as large.

The micro-instability driven transport by electrostatic fluctuations have shown to greatly affect the j_{bs} profile. Nonetheless, the existence of turbulence

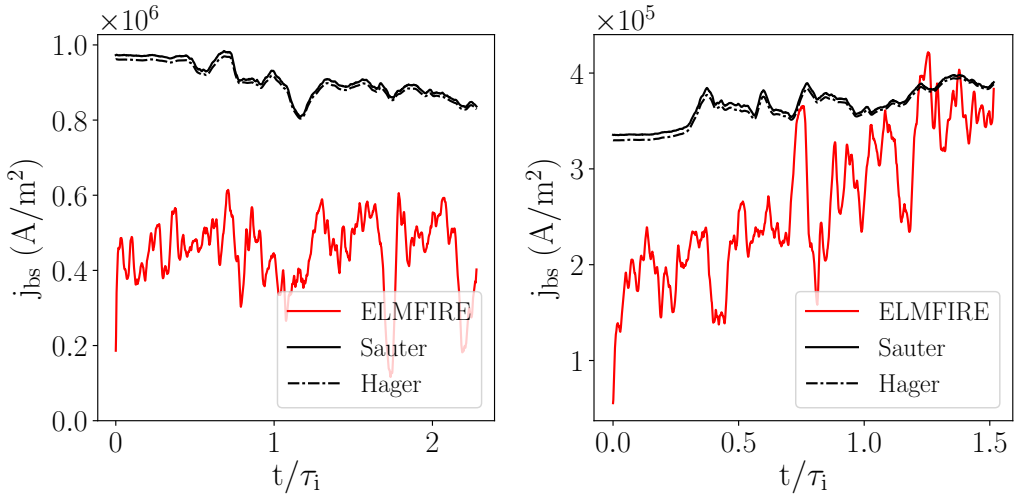

(a) (b)

Figure 5.14: Time evolution of the bootstrap current density with TEM dominated turbulence included (a) at the middle of the pedestal at $r/a \approx 0.91$ where $\tau_i \approx 150$ μs and (b) near the edge at $r/a \approx 0.96$ where $\tau_i \approx 220$ μs. The j_{bs} simulated with ELMFIRE is compared to the analytical estimates by Sauter and Hager as a function of normalized time.

was further established by considering the fluctuation amplitude and χ_i for the investigated TEM case. In the middle of the pedestal, the electrostatic fluctuation amplitude was $|e\delta\Phi/T_e| \approx 0.06$ which indicates a significant contribution from the turbulent fluctuations to the plasma current drive. The same amplitude was calculated for the ITG case. The ion heat transport coefficient χ_i oscillates around the value 2 m^2/s which is stronger than the neoclassical equivalent that stays approximately below 0.5 m^2/s.

Chapter 6

Conclusions

In this thesis, the bootstrap current profile corresponding to the steep pedestal region of a tokamak plasma was studied with both neoclassical and turbulent simulations performed using the gyrokinetic code ELMFIRE. The simulations used parameters corresponding to the JET pedestal conditions in the low collisionality banana regime. The results of the neoclassical bootstrap current density, j_{bs}, simulations were verified against two different analytical models by Sauter and Hager, and the effect of electrostatic turbulence on j_{bs} was investigated with the performed turbulent transport simulations.

As part of its diagnostics, ELMFIRE calculates the neoclassical bootstrap current density profile according to the analytical formula by Sauter, while the Hager formula was implemented in the code as part of this thesis. In the studied banana regime, the two theoretical estimates agree within 5% in the base case. The Hager model estimates larger j_{bs} than the Sauter model in the pedestal. However, increasing the collisionality closer to the plateau regime and including current damping effects from the Shafranov shift, Δ_R, into the Hager model lead to differences in j_{bs} ranging from 5% to 24% between the models when the Shafranov shift was increased from $\Delta_R = 0.1$ to 0.5. In this case, the Hager model consistently estimated lower j_{bs} than the Sauter model, and the magnitude of the difference increased linearly with respect to the Shafranov shift size.

In the neoclassical ELMFIRE simulations, the simulation predictions showed quantitative agreement with both analytical estimates in the pedestal. The differences between the two analytical models in the low-collisionality banana regime were negligible, and the ELMFIRE predictions converged to the analytical models within numerical accuracy. Discrepancies of up to 25% between the simulation and analytical estimates were, however, observed near the inner boundary of the simulation domain which are likely the result of inaccuracies introduced by the set boundary conditions. On the other

hand, the effects from the boundary conditions on j_{bs} were negligible at the outer boundary. In addition, the simulations omitted the scrape-off layer from consideration. Including SOL in ELMFIRE simulations is expected to enhance transport in the edge plasma and slightly alter the temperature and density profiles in that region, but because the analytical estimates are calculated from the profiles obtained from ELMFIRE, these modifications in the plasma would not affect the agreement between the models and simulation.

The number of binary collision grid cells used by ELMFIRE to simulate Coulomb collisions affected the accuracy of the numerical j_{bs} results. With too few collision cells, the simulated j_{bs} converged to considerably lower steady-state values than the analytical estimates, and relative differences as large as 20% were observed. The results suggest that large changes in the background temperature within a collision cell in the pedestal can introduce significant non-locality in the velocities of a colliding particle pair which reduces the accuracy of the simulation. The simulation requires a sufficient number of binary collision cells to reach adequate temperature resolution. The inaccuracies of individual particle velocities accumulate in the estimated parallel flow velocity which is used for calculating the bootstrap current density from simulation.

The Sauter formula is relatively accurate to estimate j_{bs} in the pedestal plasma with low collisionality while the local approximation required by neoclassical theory is satisfied. However, the accuracy of the model is no longer guaranteed when the gradients in the plasma profiles are increased, breaking the neoclassical assumptions as the gradient scale lengths become comparable to the ion banana orbit width. The Hager formula, on the other hand, is accurate in this non-local regime as well, thus overcoming the limitations of the Sauter model. Nevertheless, as was observed in the local regime, the results in this work showed only insignificant discrepancies between the two models also in the non-local case. ELMFIRE matches both analytical estimates well within numerical accuracy in the studied parameter regime. More significant differences between the models can be expected with larger collisionality and with effects from the Shafranov shift included, but currently, ELMFIRE simulations do not take the Shafranov shift into account.

Including electrostatic turbulence in the pedestal plasma simulations affected both the numerical and the analytical bootstrap current density profiles, which showed significant discrepancies of up to 50% between them in the middle of the pedestal. The results did not match each other as well as in the neoclassical case. Some of the disagreement is likely to result from the observed strong turbulence that affects the current drive. However, the results also suggest that with a longer simulation time, which includes multiple ion

collision times, the agreement improves. On the other hand, on such long time scales, the original profiles also change due to profile relaxation if realistic sources and sinks are not included in the simulation. Due to computational limitations, the turbulence simulations in this work did not reach convergence. At the inner boundary of the studied domain, the simulation also experienced numerical issues which possibly resulted from an inaccuracy in the reflective particle boundary condition that may not conserve energy. Consequently, the temperature at the boundary was observed to increase and the velocities of the particles were affected accordingly, which was even able to reverse the direction of the simulated bootstrap current.

Bibliography

[1] J. Wesson, *Tokamaks*. Oxford University Press, 2011, ISBN: 9780199592234.

[2] F. Wagner, G. Becker, K. Behringer, D. Campbell, A. Eberhagen, W. Engelhardt, G. Fussmann, O. Gehre, J. Gernhardt, G.v. Gierke, G. Haas, M. Huang, F. Karger, M. Keilhacker, O. Klüber, M. Kornherr, K. Lackner, G. Lisitano, G.G. Lister, H.M. Mayer, D. Meisel, E.R. Müller, H. Murmann, H. Niedermeyer, W. Poschenrieder, H. Rapp, H. Röhr, F. Schneider, G. Siller, E. Speth, A. Stäbler, K.H. Steuer, G. Venus, O. Vollmer, and Z. Yü, "Regime of Improved Confinement and High Beta in Neutral-Beam-Heated Divertor Discharges of the ASDEX Tokamak", *Physical Review Letters*, vol. 49, no. 19, pp. 1408–1412, 1982. DOI: 10.1103/PhysRevLett.49.1408.

[3] P.B. Snyder, H.R. Wilson, J.R. Ferron, L.L. Lao, A.W. Leonard, T.H. Osborne, A.D. Turnbull, D. Mossessian, M. Murakami, and X.Q. Xu, "Edge localized modes and the pedestal: A model based on coupled peeling-ballooning modes", *Physics of Plasmas*, vol. 9, no. 5, pp. 2037–2043, 2002. DOI: 10.1063/1.1449463.

[4] J.D. Lawson, "Some Criteria for a Power Producing Thermonuclear Reactor", *Proceedings of the Physical Society. Section B*, vol. 70, no. 1, pp. 6–10, 1957. DOI: 10.1088/0370-1301/70/1/303.

[5] P. Helander and D.J. Sigmar, *Collisional Transport in Magnetized Plasmas*. Cambridge University Press, 2005, ISBN: 9780521020985.

[6] J.D. Huba, *NRL Plasma Formulary*. Washington, DC: Naval Research Laboratory, 2016.

[7] F.L. Hinton and R.D. Hazeltine, "Theory of plasma transport in toroidal confinement systems", *Reviews of Modern Physics*, vol. 48, no. 2, pp. 239–308, 1976. DOI: 10.1103/RevModPhys.48.239.

[8] E. Viezzer, E. Fable, M. Cavedon, C. Angioni, R. Dux, F.M. Laggner, M. Bernert, A. Burckhart, R.M. McDermott, T. Pütterich, F. Ryter, M. Willensdorfer, E. Wolfrum, and the ASDEX Upgrade Team and the EUROfusion MST1 Team, "Investigation of inter-ELM ion heat transport in the H-mode pedestal of ASDEX Upgrade plasmas", *Nuclear Fusion*, vol. 57, no. 2, p. 022 020, 2016. DOI: 10.1088/0029-5515/57/2/022020.

[9] J. Weiland, *Collective Modes in Inhomogeneous Plasma: Kinetic and Advanced Fluid Theory*. Institute of Physics Publishing, 2000, ISBN: 9780750305891.

[10] C.J. McDevitt, Xian-Zhu Tang, and Zehua Guo, "Turbulent current drive mechanisms", *Physics of Plasmas*, vol. 24, no. 8, p. 082 307, 2017. DOI: 10.1063/1.4996222.

[11] M. Kikuchi and M. Azumi, "Experimental evidence for the bootstrap current in a tokamak", *Plasma Physics and Controlled Fusion*, vol. 37, no. 11, pp. 1215–1238, 1995. DOI: 10.1088/0741-3335/37/11/003.

[12] D.M. Thomas, A.W. Leonard, L.L. Lao, T.H. Osborne, H.W. Mueller, and D.F. Finkenthal, "Measurement of Pressure-Gradient-Driven Currents in Tokamak Edge Plasmas", *Physical Review Letters*, vol. 93, no. 6, p. 065 003, 2004. DOI: 10.1103/PhysRevLett.93.065003.

[13] R.J. Bickerton, J.W. Connor, and J.B. Taylor, "Diffusion Driven Plasma Currents and Bootstrap Tokamak", *Nature Physical Science*, vol. 229, no. 4, pp. 110–112, 1971. DOI: 10.1038/physci229110a0.

[14] A.G. Peeters, "Bootstrap current and its consequences", *Plasma Physics and Controlled Fusion*, vol. 42, no. 12B, B231–B242, 2000. DOI: 10.1088/0741-3335/42/12B/318.

[15] O. Sauter, C. Angioni, and Y.R. Lin-Liu, "Neoclassical conductivity and bootstrap current formulas for general axisymmetric equilibria and arbitrary collisionality regime", *Physics of Plasmas*, vol. 6, no. 7, pp. 2834–2839, 1999. DOI: 10.1063/1.873240.

[16] O. Sauter, C. Angioni, and Y.R. Lin-Liu, "Erratum: "Neoclassical conductivity and bootstrap current formulas for general axisymmetric equilibria and arbitrary collisionality regime" [Phys. Plasmas 6, 2834 (1999)]", *Physics of Plasmas*, vol. 9, no. 12, p. 5140, 2002. DOI: 10.1063/1.1517052.

[17] S.P. Hirshman, "Finite-aspect-ratio effects on the bootstrap current in tokamaks", *Physics of Fluids*, vol. 31, no. 10, pp. 3150–3152, 1988. DOI: 10.1063/1.866973.

[18] C.E. Kessel, "Bootstrap current in a tokamak", *Nuclear Fusion*, vol. 34, no. 9, p. 1221, 1994. DOI: 10.1088/0029-5515/34/9/I04.

[19] S. Koh, C.S. Chang, S. Ku, J.E. Menard, H. Weitzner, and W. Choe, "Bootstrap current for the edge pedestal plasma in a diverted tokamak geometry", *Physics of Plasmas*, vol. 19, no. 7, p. 072 505, 2012. DOI: 10.1063/1.4736953.

[20] E.A. Belli, J. Candy, O. Meneghini, and T.H. Osborne, "Limitations of bootstrap current models", *Plasma Physics and Controlled Fusion*, vol. 56, no. 4, p. 045 006, 2014. DOI: 10.1088/0741-3335/56/4/045006.

[21] R. Hager and C.S. Chang, "Gyrokinetic neoclassical study of the bootstrap current in the tokamak edge pedestal with fully non-linear Coulomb collisions", *Physics of Plasmas*, vol. 23, no. 4, p. 042 503, 2016. DOI: 10.1063/1.4945615.

[22] C.J. McDevitt, Xian-Zhu Tang, and Zehua Guo, "Turbulence-Driven Bootstrap Current in Low-Collisionality Tokamaks", *Physical Review Letters*, vol. 111, no. 20, p. 205 002, 2013. DOI: 10.1103/PhysRevLett.111.205002.

[23] J.A. Heikkinen, S.J. Janhunen, T.P. Kiviniemi, and F. Ogando, "Full f gyrokinetic method for particle simulation of tokamak transport", *Journal of Computational Physics*, vol. 227, no. 11, pp. 5582–5609, 2008. DOI: 10.1016/j.jcp.2008.02.013.

[24] T. Korpilo, A.D. Gurchenko, E.Z. Gusakov, J.A. Heikkinen, S.J. Janhunen, T.P. Kiviniemi, S. Leerink, P. Niskala, and A.A. Perevalov, "Gyrokinetic full-torus simulations of ohmic tokamak plasmas in circular limiter configuration", *Computer Physics Communications*, vol. 203, pp. 128–137, 2016. DOI: 10.1016/j.cpc.2016.02.021.

[25] C.K. Birdsall and A.B. Langdon, *Plasma Physics via Computer Simulation*. CRC Press, 2004, ISBN: 9780750310253.

[26] T. Takizuka and H. Abe, "A binary collision model for plasma simulation with a particle code", *Journal of Computational Physics*, vol. 25, no. 3, pp. 205–219, 1977. DOI: 10.1016/0021-9991(77)90099-7.

[27] S. Ma, R.D. Sydora, and J.M. Dawson, "Binary collision model in gyrokinetic simulation plasmas", *Computer Physics Communications*, vol. 77, no. 2, pp. 190–206, 1993. DOI: 10.1016/0010-4655(93)90003-U.

[28] X. Garbet, Y. Idomura, L. Villard, and T.H. Watanabe, "Gyrokinetic simulations of turbulent transport", *Nuclear Fusion*, vol. 50, no. 4, p. 043 002, 2010. DOI: 10.1088/0029-5515/50/4/043002.

[29] T. Korpilo, T.P. Kiviniemi, S. Leerink, P. Niskala, and R. Rochford, "Gyrokinetic Simulations of the Tokamak Plasma Edge in Circular Limiter Configuration", *Contributions to Plasma Physics*, vol. 56, no. 6-8, pp. 549–554, 2016. DOI: 10.1002/ctpp.201610046.

[30] T. Korpilo, "Global Gyrokinetic Particle Simulations of Circular Limiter Tokamak Plasmas", PhD thesis, Aalto University, Espoo, 2017, ISBN: 9789526075617.

[31] T.P. Kiviniemi, S. Leerink, P. Niskala, J.A. Heikkinen, T. Korpilo, and S. Janhunen, "Comparison of gyrokinetic simulations of parallel plasma conductivity with analytical models", *Plasma Physics and Controlled Fusion*, vol. 56, no. 7, p. 075 009, 2014. DOI: 10.1088/0741-3335/56/7/075009.

[32] M. Greenwald, "Verification and validation for magnetic fusion", *Physics of Plasmas*, vol. 17, no. 5, p. 058 101, 2010. DOI: 10.1063/1.3298884.

[33] M.N.A. Beurskens, T.H. Osborne, L.D. Horton, L. Frassinetti, R. Groebner, A. Leonard, P. Lomas, I. Nunes, S. Saarelma, P.B. Snyder, I. Balboa, B. Bray, K. Crombé, J. Flanagan, C. Giroud, E. Giovannozzi, M. Kempenaars, N. Kohen, A. Loarte, J. Lönnroth, E. de la Luna, G. Maddison, C. Maggi, D. McDonald, G. McKee, R. Pasqualotto, G. Saibene, R. Sartori, E. Solano, W. Suttrop, E. Wolfrum, M. Walsh, Z. Yan, L. Zabeo, D. Zarzoso, and JET-EFDA contributors, "Pedestal width and ELM size identity studies in JET and DIII-D; implications for ITER", *Plasma Physics and Controlled Fusion*, vol. 51, no. 12, p. 124 051, 2009. DOI: 10.1088/0741-3335/51/12/124051.

[34] C. Wang, T. Lin, R. Caflisch, B.I. Cohen, and A.M. Dimits, "Particle simulation of Coulomb collisions: Comparing the methods of Takizuka & Abe and Nanbu", *Journal of Computational Physics*, vol. 227, no. 9, pp. 4308–4329, 2008. DOI: 10.1016/j.jcp.2007.12.027.

[35] A.M. Dimits, C. Wang, R. Caflisch, B.I. Cohen, and Y. Huang, "Understanding the accuracy of Nanbu's numerical Coulomb collision operator", *Journal of Computational Physics*, vol. 228, no. 13, pp. 4881–4892, 2009. DOI: 10.1016/j.jcp.2009.03.041.

[36] P. Niskala, T.P. Kiviniemi, S. Leerink, and T. Korpilo, "Gyrokinetic simulations of interplay between geodesic acoustic modes and trapped electron mode turbulence", *Nuclear Fusion*, vol. 55, no. 7, p. 073 012, 2015. DOI: 10.1088/0029-5515/55/7/073012.

[37] R.B. White, *The Theory of Toroidally Confined Plasmas*. Imperial College Press, 2001, ISBN: 9781860946394.

Appendix A

Equations of motion

The equations for the guiding center drift particle motion in ELMFIRE are derived in this appendix using the Lagrangian formalism. These equations allow for accurate integration of particle parallel velocity which is crucial for calculating the bootstrap current. The equations are given in general form in Ref. [30] but are here derived rigorously and expressed in their final form. ELMFIRE uses a set of Boozer coordinates where the conventionally used equation for $d\rho_\parallel/dt$ [37] is replaced with $dv_\parallel/dt$ which makes implicit evaluation of the electron parallel motion more straightforward.

We start by considering the guiding center one-form given by

$$\Gamma_{\mathrm{gc}} = q_e \left(\bar{A} + \rho_\parallel \bar{B}\right) \cdot d\bar{x} \tag{A.1}$$

where q_e is the particle charge and $\rho_\parallel = v_\parallel/\Omega$ is the parallel gyroradius with $v_\parallel$ being the parallel speed and $\Omega = q_e B/m$ the gyrofrequency, B is the magnetic field strength and m is the particle mass. The magnetic field and the vector potential are defined as

$$\bar{B} = \nabla\psi \times \nabla\theta + \nabla\phi \times \nabla\psi_p = I\nabla\theta + g\nabla\phi \tag{A.2}$$

$$\bar{A} = \psi\nabla\theta - \psi_p\nabla\phi \tag{A.3}$$

where ψ and ψ_p are the toroidal and poloidal magnetic fluxes, and ϕ and θ are the toroidal and poloidal angles, respectively. $I = \mu_0 I_{\mathrm{p}}$ with μ_0 being the vacuum permeability and I_{p} the plasma current, and $g = R_0 B_t$ with R_0 being the major radius and B_t the toroidal magnetic field strength. The two terms in the one-form equation can be rewritten using the definitions for $\bar{B}$ and $\bar{A}$, and the relation $\nabla\theta \cdot d\bar{x} = \nabla\theta \cdot \frac{\partial\bar{x}}{\partial u} \cdot du = d\theta$ to get

$$q_e \bar{A} \cdot d\bar{x} = q_e \left(\psi d\theta - \psi_p d\phi\right) \tag{A.4}$$

$$q_e \rho_\parallel \bar{B} \cdot d\bar{x} = q_e \frac{v_\parallel}{\Omega} \left(I d\theta + g d\phi\right) \tag{A.5}$$

and adding the terms together yields

$$\Gamma_{\mathrm{gc}} = q_e \left(\psi + \frac{v_\parallel}{\Omega} I\right) d\theta + q_e \left(\frac{v_\parallel}{\Omega} g - \psi_p\right) d\phi. \tag{A.6}$$

Next, the guiding center two-form is defined as

$$\omega_{\mathrm{gc}} = d\Gamma_{\mathrm{gc}} \tag{A.7}$$

and for the differentiation we use the relation $d(\Phi\, dx) = \partial_j \Phi\, du^j \wedge dx$ where for example $\partial_j = \partial/\partial\psi_p$, $du^j = d\psi_p$. In addition, the safety factor is $q_s = \partial\psi/\partial\psi_p$ and $\psi = \psi(\psi_p)$, $q_s = q_s(\psi_p)$, $I = I(\psi_p)$, $g = g(\psi_p)$, and $\Omega = \Omega(B(\psi_p, \theta))$ i.e. axisymmetric magnetic field is assumed. By differentiating the terms of the one-form equation we get the two-form terms which are

$$d(q_e \psi d\theta) = q_e d\left(\psi d\theta\right) = q_e \frac{\partial \psi}{\partial \psi_p} d\psi_p \wedge d\theta = q_e q_s d\psi_p \wedge d\theta \tag{A.8}$$

$$\begin{aligned}
&d\left(q_e \frac{v_\parallel}{\Omega} I d\theta\right) = m d\left(\frac{v_\parallel}{B} I d\theta\right) \\
&= m\left(v_\parallel \frac{\partial}{\partial \psi_p}\left(\frac{I}{B}\right) d\psi_p \wedge d\theta + v_\parallel I \frac{\partial}{\partial \theta}\left(\frac{1}{B}\right) d\theta \wedge d\theta + \frac{I}{B}\frac{\partial v_\parallel}{\partial v_\parallel} dv_\parallel \wedge d\theta\right) \\
&= m\left(v_\parallel \left[\left(I'B - IB'\right)/B^2\right] d\psi_p \wedge d\theta + \frac{I}{B} dv_\parallel \wedge d\theta\right) \\
&= \frac{m v_\parallel}{B^2}\left(I'B - IB'\right) d\psi_p \wedge d\theta + \frac{mI}{B} dv_\parallel \wedge d\theta
\end{aligned} \tag{A.9}$$

$$\begin{aligned}
&d\left(q_e \frac{v_\parallel}{\Omega} g d\phi\right) = m d\left(\frac{v_\parallel}{B} g d\phi\right) \\
&= m\left(v_\parallel \frac{\partial}{\partial \psi_p}\left(\frac{g}{B}\right) d\psi_p \wedge d\phi + v_\parallel g \frac{\partial}{\partial \theta}\left(\frac{1}{B}\right) d\theta \wedge d\phi + \frac{g}{B}\frac{\partial v_\parallel}{\partial v_\parallel} dv_\parallel \wedge d\phi\right) \\
&= m\left(v_\parallel \left[\left(g'B - gB'\right)/B^2\right] d\psi_p \wedge d\phi - \frac{v_\parallel g}{B^2}\frac{\partial B}{\partial \theta} d\theta \wedge d\phi + \frac{g}{B} dv_\parallel \wedge d\phi\right) \\
&= \frac{m v_\parallel}{B^2}\left(g'B - gB'\right) d\psi_p \wedge d\phi - \frac{m v_\parallel g}{B^2}\frac{\partial B}{\partial \theta} d\theta \wedge d\phi + \frac{mg}{B} dv_\parallel \wedge d\phi
\end{aligned} \tag{A.10}$$

$$d\left(-q_e \psi_p d\phi\right) = -q_e d\left(\psi_p d\phi\right) = -q_e \frac{\partial \psi_p}{\partial \psi_p} d\psi_p \wedge d\phi = -q_e d\psi_p \wedge d\phi \tag{A.11}$$

where prime denotes differentiation with respect to ψ_p. Now we can assemble the Lagrangian matrix ω_{gc} which is by definition antisymmetric and has zeros on the diagonal

$$\omega_{\rm gc} = \left| \begin{array}{cccc|c} \psi_p & \theta & \phi & v_\parallel & \\ 0 & a & b & 0 & \psi_p \\ -a & 0 & c & d & \theta \\ -b & -c & 0 & e & \phi \\ 0 & -d & -e & 0 & v_\parallel \end{array} \right|$$

where $a = q_e q_s + m v_\parallel / B^2 (I'B - IB')$, $b = -q_e + m v_\parallel / B^2 (g'B - gB')$, $c = \left(-m v_\parallel g / B^2\right) \partial B / \partial \theta$, $d = -mI/B$, and $e = -mg/B$. The matrix is then inverted $J_{\rm gc} = \omega_{\rm gc}^{-1}$ which yields

$$J_{\rm gc} = \frac{1}{D} \left| \begin{array}{cccc} 0 & e & -d & c \\ -e & 0 & 0 & -b \\ d & 0 & 0 & a \\ -c & b & -a & 0 \end{array} \right|$$

where $D = bd - ae = m q_e / B (I + q_s g) + m^2 v_\parallel / B^2 (I'g - Ig')$ is the determinant.

The equations of motion are defined as $dx_\alpha / dt = \{x_\alpha, H\} = J^{\alpha\beta} \partial H / \partial x_\beta$ where $x = \{\psi_p, \theta, \phi, v_\parallel\}$ and H is the Hamiltonian. For the guiding center drift motion the Hamiltonian is defined as

$$H = \frac{m v_\parallel^2}{2} + \mu B + q_e \Phi \tag{A.12}$$

where μ is the magnetic moment, and Φ is the electric potential, with $B = B(\psi_p, \theta)$ and $\Phi = \Phi(\psi_p, \theta, \phi)$. We can now solve the equations of motion which are

$$\begin{aligned} \frac{d\psi_p}{dt} &= -\frac{1}{D} \frac{mg}{B} \left(\mu \frac{\partial B}{\partial \theta} + q_e \frac{\partial \Phi}{\partial \theta} \right) + \frac{1}{D} \frac{mI}{B} q_e \frac{\partial \Phi}{\partial \phi} - \frac{1}{D} \frac{m v_\parallel g}{B^2} \frac{\partial B}{\partial \theta} m v_\parallel \\ &= -\frac{g}{D} \left(\frac{m}{B} \mu + \frac{m^2 v_\parallel^2}{B^2} \right) \frac{\partial B}{\partial \theta} + \frac{I}{D} \frac{m}{B} q_e \frac{\partial \Phi}{\partial \phi} - \frac{g}{D} \frac{m}{B} q_e \frac{\partial \Phi}{\partial \theta} \end{aligned} \tag{A.13}$$

$$\begin{aligned} \frac{d\theta}{dt} &= \frac{1}{D} \frac{mg}{B} \left(\mu \frac{\partial B}{\partial \psi_p} + q_e \frac{\partial \Phi}{\partial \psi_p} \right) + \frac{1}{D} \left(q_e - \frac{m v_\parallel}{B} g' + \frac{m v_\parallel}{B^2} g B' \right) m v_\parallel \\ &= \frac{m v_\parallel}{D} \left(q_e - \frac{m v_\parallel}{B} g' \right) + \left(\frac{m}{B} \mu + \frac{m^2 v_\parallel^2}{B^2} \right) \frac{g}{D} \frac{\partial B}{\partial \psi_p} + \frac{g}{D} \frac{m}{B} q_e \frac{\partial \Phi}{\partial \psi_p} \end{aligned} \tag{A.14}$$

$$\begin{aligned}\frac{d\phi}{dt} &= -\frac{1}{D}\frac{mI}{B}\left(\mu\frac{\partial B}{\partial\psi_p}+q_e\frac{\partial\Phi}{\partial\psi_p}\right)+\frac{1}{D}\left(q_eq_s+\frac{mv_\parallel}{B}I'-\frac{mv_\parallel}{B^2}IB'\right)mv_\parallel \\ &= \frac{mv_\parallel}{D}\left(q_eq_s+\frac{mv_\parallel}{B}I'\right)-\left(\frac{m}{B}\mu+\frac{m^2v_\parallel^2}{B^2}\right)\frac{I}{D}\frac{\partial B}{\partial\psi_p}-\frac{I}{D}\frac{m}{B}q_e\frac{\partial\Phi}{\partial\psi_p} \qquad \text{(A.15)}\end{aligned}$$

$$\begin{aligned}\frac{dv_\parallel}{dt} &= \frac{1}{D}\frac{mv_\parallel g}{B^2}\frac{\partial B}{\partial\theta}\left(\mu\frac{\partial B}{\partial\psi_p}+q_e\frac{\partial\Phi}{\partial\psi_p}\right) \\ &\quad+\frac{1}{D}\left(\frac{mv_\parallel}{B}g'-\frac{mv_\parallel}{B^2}gB'-q_e\right)\left(\mu\frac{\partial B}{\partial\theta}+q_e\frac{\partial\Phi}{\partial\theta}\right) \\ &\quad+\frac{1}{D}\left(-q_eq_s-\frac{mv_\parallel}{B}I'+\frac{mv_\parallel}{B^2}IB'\right)q_e\frac{\partial\Phi}{\partial\phi} \\ &= -\frac{1}{D}\left(q_e\mu-\frac{mv_\parallel}{B}\mu g'-\frac{mv_\parallel}{B^2}q_eg\Phi'\right)\frac{\partial B}{\partial\theta} \\ &\quad-\frac{1}{D}\left(q_e^2-\frac{mv_\parallel}{B}q_eg'+\frac{mv_\parallel}{B^2}q_egB'\right)\frac{\partial\Phi}{\partial\theta} \\ &\quad-\frac{1}{D}\left(q_e^2q_s+\frac{mv_\parallel}{B}q_eI'-\frac{mv_\parallel}{B^2}q_eIB'\right)\frac{\partial\Phi}{\partial\phi} \qquad \text{(A.16)}\end{aligned}$$